

# Measurement of $\mu$ Life-Time and $\hat{P}$ -Violation in Polarized Muon Decay

Raffaele Gerosa    Badder Marzocchi    Luca Mastrolorenzo

*University of Milano-Bicocca*

September 19, 2011

## Abstract

After a characterization of the experimental equipment, the experiment is performed in two stages. In the first one the aim is the  $\mu$  lifetime measurement in vacuum and in different materials (*Al* and *NaCl*), giving the following results:  $\tau = 2.193 \pm 0.048(stat) \pm 0.058(syst)$   $\mu s$  and  $\tau = 2.194 \pm 0.026(stat) \pm 0.145(syst)$   $\mu s$  for the vacuum,  $\tau(Al) = 870 \pm 93(stat) \pm 35(syst)$   $ns$  and  $\tau(NaCl) = 702 \pm 136(stat) \pm 52(syst)$   $ns$ . In the second one, the goal is to probe weak  $\hat{P}$ -violation through asymmetry oscillation measurement in  $\mu$  polarized decay in magnetic field. Through this method we manage to exclude within 90% C.L. the absence of asymmetry oscillation and to confirm it within 46.33%  $\chi^2$ -significance.

## 1 Introduction

In the first section Sec.1.1, the main features of cosmic muons are presented; then in 1.2 and 1.3 the attention is focused on free and bound muon decay in matter.

### 1.1 Cosmic Rays

Muon is a charged particle belonging to the second leptonic family. It is like the electron except for its rest mass:

$$m_\mu = 105.6583668 \pm 0.0000038 MeV [1]$$

Muons observed in our laboratory have cosmic origin. Cosmic rays are particles coming from outer space and are divided into two main families: "primary" and "secondary" cosmic rays. Particles belonging to the primary one have extra-galactic origin and are composed mainly by protons ( $\sim 95\%$ ), He nuclei ( $\sim 5\%$ ) and in a small number of light charged particles and antiparticles. Thus electrons, protons and helium, as well as carbon, oxygen, iron, and other nuclei synthesized in stars, are primaries. It's possible to estimate their differential energy spectrum, reported in Fig.1, with polynomial functions [2], [3]:

$$\frac{dN}{dE} \approx \begin{cases} const \cdot E^{-3.1} & E/c < 100 PeV/c \\ const \cdot E^{-2.7} & E/c > 100 PeV/c \end{cases} \quad (1)$$

Particles belonging to the "secondary" family are generated by interactions of the primaries with interstellar gas, in our specific case with Earth's upper atmosphere. These interactions create mainly pions ( $\pi^+, \pi^0, \pi^-$ ) and photons ( $\gamma$ ), minimally kaons ( $K^+, K^0, K^-$ ) and other particles and nuclei such as lithium, beryllium, and boron. Pions and kaons are unstable particles and

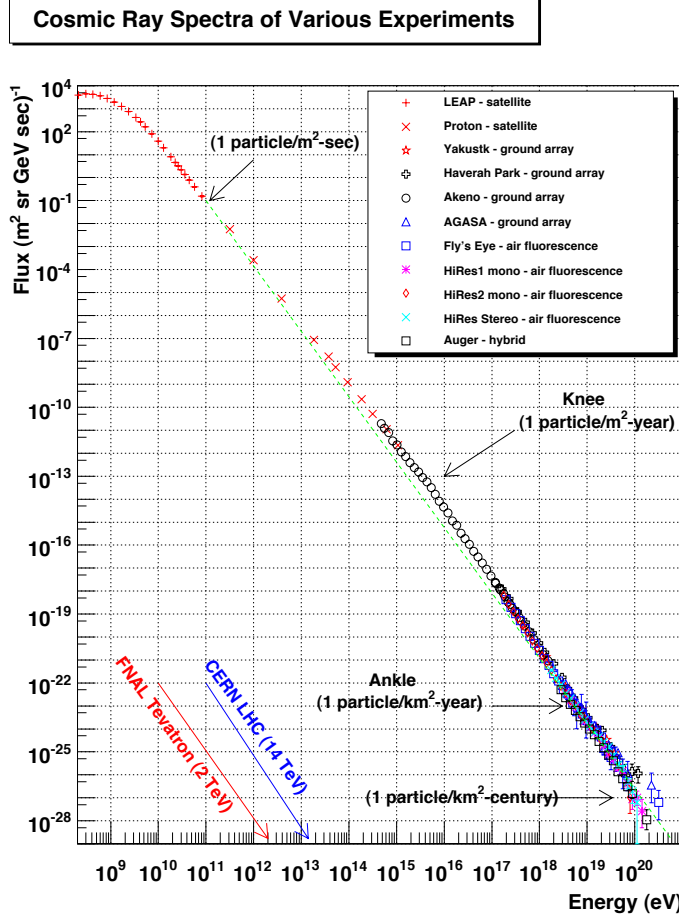


Figure 1: Spectrum of primary cosmic rays.

decay into lighter ones. These processes form two types of showers: the electromagnetic and the hadronic ones. E.g. we report some of the main reactions:

$$p + X \rightarrow \pi^{\pm(0)} + Y, \quad \pi^0 \rightarrow \gamma + \gamma, \quad \gamma \rightarrow e^+ + e^-, \quad Y \rightarrow n + p, \quad \pi^\pm \rightarrow \mu^\pm + \nu_\mu (\bar{\nu}_\mu)$$

The majority of the decay products cannot reach the Earth's surface because they have a too short lifetime and not enough energy. On the other hand, most of the muons and all neutrinos, produced by charged pions decay, can easily reach the surface. So, muons are the most plentiful charged particles at the sea level. They are produced in the high atmosphere (typically 15 km) and they lose about 2 GeV by ionization before reaching the ground. As muon is not the lightest lepton, it decays into:

$$\mu^- \rightarrow e^- + \bar{\nu}_e + \nu_\mu \quad \mu^+ \rightarrow e^+ + \nu_e + \bar{\nu}_\mu$$

Its mean free lifetime is reported beneath:

$$\tau_\mu = (2.197034 \pm 0.000021) \times 10^{-6} s [1] \quad (2)$$

Because of the muons are produced at about 15 Km in the atmosphere, they can reach the sea level only if:

$$\gamma = \frac{L}{c\tau_\mu} \approx 23 \quad E = m_0 c^2 \gamma \approx 2.4 \text{ GeV} \left( + 2 \text{ GeV loss by ionization} \right) \rightarrow E \geq 4 \text{ GeV}$$

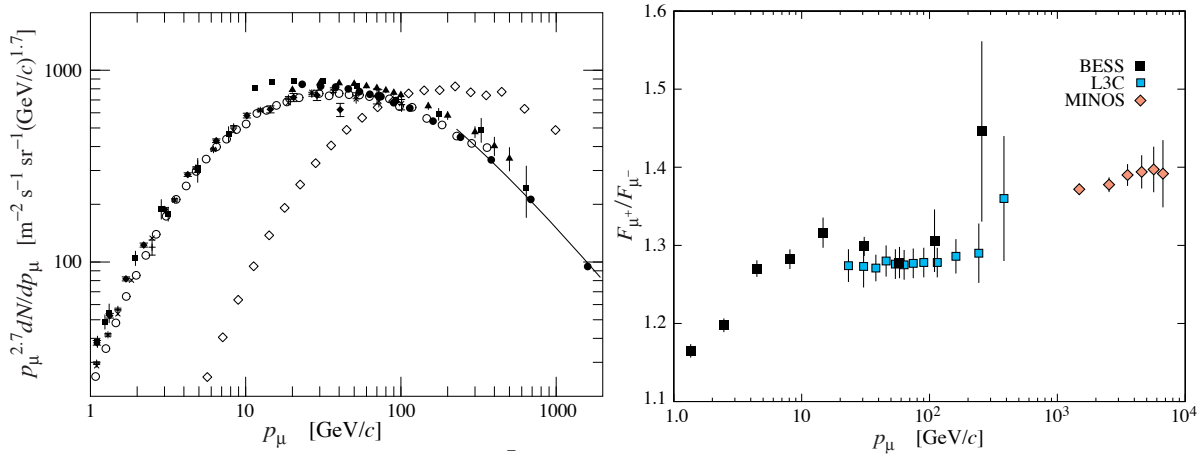


Figure 2: *Left:* spectrum of muons at  $\theta = 75^\circ$  ( $\diamond$ ) and  $\theta = 0^\circ$  (all the other symbols)[1]. *Right:* cosmic muons charge asymmetry, measured at sea level [1].

The mean energy of muons at the ground is approximately 4 GeV, as reported in [1]. The energy spectrum over 1 GeV is shown in Fig.2, whereas it is almost flat below 1 GeV. The flux of vertical muons above 1 GeV at the sea level is

$$\phi_\mu(\theta = 0^\circ) \approx 1 \text{ cm}^{-2} \text{ min}^{-1} \quad [1]. \quad (3)$$

The angular distribution at sea level for muons with energy above 3 GeV is:

$$\frac{dN}{d\Omega dAdt} \approx I_0 \cos^2 \theta \quad I_0 \approx 100 \text{ m}^{-2} \text{ sr}^{-1} \text{ s}^{-1} \quad (4)$$

Another important feature of cosmic muons is their measured charge asymmetry, reported in Fig.2. This asymmetry is due to the excess of protons over neutrons in the primary spectrum, which brings an overabundance of  $\pi^+$  over  $\pi^-$ .

## 1.2 Free Muon Decay

This is a fully leptonic process in which a muon ( $q_\mu = e$  and momentum  $p_\mu$ ) is converted into an electron ( $m_e = 0.511 \text{ MeV}$ ,  $p_e$ ) through the emission of two neutrinos ( $p_{\nu_e}, p_{\bar{\nu}_\mu}$ ):

$$\mu^- \longrightarrow e^- + \bar{\nu}_e + \nu_\mu \quad \text{or} \quad \mu^+ \longrightarrow e^+ + \nu_e + \bar{\nu}_\mu$$

The process is described by the Feynman graph in Fig.3. The decay rate  $\Gamma$  is given by:

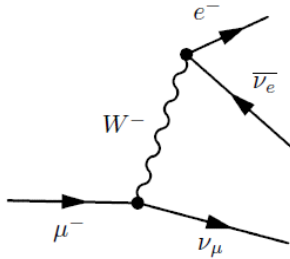


Figure 3: Feynmann graph for muon decay at LO.

$$d\Gamma = (2\pi)^4 \delta^4 \left( p_\mu - \sum_f p_f \right) \frac{1}{2E_\mu} \prod_f \frac{d^3 p_f}{(2\pi)^3 2E_f} \sum_f |M|^2 \quad (5)$$

where  $f=\{1,2,3\}$  is the final state particles index ( $e$ ,  $\nu_e$  and  $\nu_\mu$ ). The amplitude  $M$  follows from the Feynman rules. Making all the calculations described in Appendix A:

$$\Gamma = \frac{G_f^2 m_\mu^5}{192\pi^3} \implies \tau[\mu^\pm \rightarrow e + \nu_e + \nu_\mu] = 2.2\mu s \quad (6)$$

A most accurate value for  $\tau_\mu$  is calculated taking into account: the electron mass, providing correction of order  $m_e^2/m_\mu^2$  for  $\Gamma$ , the Q.E.D radiative correction  $\Gamma^{(1)} = \Gamma^{(0)} \left[ 1 - \frac{\alpha}{2\pi} (\pi^2 - \frac{25}{4}) + O(\alpha^2) \right]$  and the B.R. of this decay mode (0.9986, against the  $1.4 \cdot 10^{-2}$  of the channel  $e^- \nu_\mu \bar{\nu}_e \gamma$  [1]). After that, the Standard Model prediction for  $\mu$  lifetime is consistent with the experimental measurements reported in Eq.2.

### 1.3 Bound Muon Decay

The composition of the muons, with  $\langle E_\mu \rangle \approx 4 \text{ GeV}$ , arriving to the sea-level is about 56%  $\mu^+$  and 44%  $\mu^-$ , see Fig.2. If we consider a material, the positive muons can cross it, releasing some of their energy; or they can be stopped and decay free, almost at rest. On the other hand, negative muons can also bind with the material atoms, making the "mu-mesic atoms". In this configuration the  $\mu^-$  can decay as if it were approximately free or it can be captured by the nucleus. If the muon binds in a non-K shell it emits X rays until it reaches the K shell. About the capture we have to note that the highest is nucleus's Z, the most is the capture probability. This can be explained if we think that the increasing of Z reduces atomic orbital radii and increases the probability that the muon can be found in the nucleus. When the muon is in the nucleus, it can weakly interact with a quark; this interaction can be summarized as:

$$p + \mu^- \rightarrow n + \nu_\mu$$

and it is represented in Fig.4. If the proton is at rest, the energy of the production neutron is

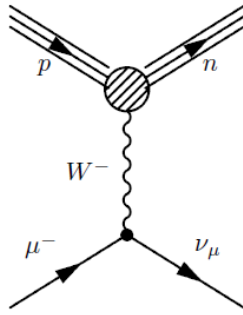


Figure 4: Feynmann graph for capture muon decay.

about 5.2 MeV [4], but as the nucleons are in constant motion, the neutron energy is about few tens of MeV. These fast neutrons either leave the nucleus, or make a direct interaction ejecting a particle or transfer their energy to other nucleus. Because of the Coulombian barrier, the emission of protons or other charged particles is impeded, so that the only products we see are neutrons and  $\gamma$  rays. There is also another possible interaction with nucleus quarks with the emission of a highly energetic  $\gamma$  ray,  $E_{peak} = 30 \text{ MeV}$  [4]:

$$p + \mu^- \rightarrow n + \nu_\mu + \gamma$$

This process is rare, indeed [4]:

$$R = \frac{\Gamma_{Rad}}{\Gamma_C} \approx 10^{-4}$$

where  $\Gamma_{Rad}$  is radiative capture rate and  $\Gamma_C$  is non-radiative one. Because of quarks interactions at low energies, the theoretical description of muon capture is very difficult and strongly model dependent. A theoretical description of this phenomenon is beyond this report goal. If  $\Gamma_C(Z)$  is non-radiative capture rate and  $\Gamma_D(Z)$  is the decay rate without nuclear interaction in  $\mu$ -mesic atoms, we have:

$$\Gamma(Z) = \Gamma_C(Z) + \Gamma_D(Z) \quad \tau^- = \frac{1}{\Gamma(Z)} \quad (7)$$

As we know, these rates depend on nucleus Z. For low  $Z \rightarrow \Gamma_D \approx \frac{1}{\tau^+}$ , whereas for high Z we have to take into account a lot of other effects. Firstly, the total energy of the bound negative muon is less than the total energy of the free positive muon because of the binding energy. Consequently the phase space is reduced, decreasing the decay probability. Secondly the effect of the nuclear Coulomb field may influence the decay probability. Finally, the motion of negative muon in the K shell gives rise to a relativistic change in the time scale, increasing the life-time in the lab. An estimation of the  $\Gamma_D(Z)$  decreasing is:

$$\Gamma_D(Z) \approx \left[ 1 - \rho \left( \frac{Z}{137} \right)^2 \right] \cdot \Gamma_D(0) \quad [4] \quad (8)$$

where  $\rho \approx 3$ ; this is valid for  $Z < \frac{137}{\sqrt{\rho}}$ . About  $\Gamma_C(Z)$  we can say that greater Z decreases orbital radii and increases nucleus dimension, so that the nucleus point-charge approximation becomes impossible. An estimation of this effect is given by Primakoff law [4]:

$$Z_{eff} = Z \left[ 1 + \left( \frac{Z}{42} \right)^{1.47} \right]^{-\frac{1}{1.47}} \quad (9)$$

The Tab.1 gives some experimental data.

| Element | Z  | $\Gamma_D(Z) (10^5 s^{-1})$ | $\Gamma(Z) (10^5 s^{-1})$ | $\tau (ns)$ |
|---------|----|-----------------------------|---------------------------|-------------|
| C       | 6  | 0.36±0.01                   | 3.97±0.01 [5]             | 2025±4 [5]  |
| Na      | 11 | 3.87±0.15                   | 8.40±0.14                 | 1190± 20    |
| Al      | 13 | 6.91±0.20                   | 11.40±0.13                | 880±10      |
| Cl      | 17 | 13.9±0.9                    | 18.5±0.68                 | 540±20      |
| Pb      | 82 | 129±5                       | 133.0±5.8                 | 75±3        |

Table 1:  $\mu^-$  experimental decay and capture rates in different materials [4].

## 2 Experimental Equipment

The aim of the experiment is to perform only time measurements, thus we need a detector able to provide a very fast response to the passage of a particle  $O(ns)$ . The precision of a time measurement is in general determined by two main factors:

- Time Jitter: it is the time dispersion of the signal caused by random effect in its formation. It is irreducible and cannot be corrected.
- Threshold Walk: it is the dispersion of the threshold crossing time due to signal amplitude fluctuations.

Knowing that, for fast detector we mean a detector producing a signal with a low jitter and short rise-time, which can give a usable information in a very short time. The simplest and most widely used detectors of this class are the organic scintillators, which have low density  $\rho \approx 1 \text{ g/cm}^3$  and a fast response time  $\approx \text{ns}$ .

In this experiment we use three organic plastic scintillators  $4.25 \times 30.30 \times 80.50 \text{ cm}$ <sup>1</sup>. Each one is coupled to a photomultiplier tube through a wavelength shifter. Moreover, the electronics used for the processing of the signal extracted at the anode of each PM is:

- One Crate NIM.
- One 8-Channel Low-Threshold Discriminator<sup>2</sup>.
- Quad logic Fan-in/Fan-out.
- One 4-fold programmable logic unit with veto<sup>3</sup>.
- One Dual Timer (Caen N93B).
- One Octal Gate and Delay Generator (Ortec GG8020).
- One Quad Coincidence Unit<sup>4</sup>.
- One NIM 4-Channel Programmable Power Supply<sup>5</sup>.
- One DC Power Supply SPS-1230, 12V-30A, GW INSTEK
- One two-channel digital oscilloscope with GPIB output.
- One PC for data acquisition and processing.

### 2.1 Interaction Muon-Scintillator

As reported in Sec.1.1, muons reach the ground with a mean energy of  $\langle E_\mu \rangle \approx 4 \text{ GeV}$ . When they cross an absorber, such as a scintillator, they lose some of their energy thanks to scattering events with the internal electrons. The energy loss per unit length, called stopping power, for a massive charged particle ( $m_\mu \gg m_e$ ) is given by the Bethe-Block equation [6]:

$$-\frac{dE}{dx} = 4\pi N_A \rho \frac{Z}{A} \frac{e^4 z^2}{m_e v^2} \left[ \ln \left( \frac{2m_e c^2 \beta^2 \gamma^2}{I} \right) - \beta^2 - \frac{\delta}{2} \right] \quad (10)$$

<sup>1</sup> <http://www.detectors.saint-gobain.com/uploadedFiles/SGdetectors/Documents/ProductDatasheets/BC400-404-408-412-416-Data-Sheet.pdf>

<sup>2</sup> CAEN model N 417, <http://www.caentechologies.com/csite/SpecialCodes.jsp>

<sup>3</sup> N405 Triple 4-Fold Logic Unit/Majority with VETO

<sup>4</sup> LeCroy 622 Quad 2 Input Logic Unit, <http://www.lecroy.com/lrs/dsheets/365al.htm>

<sup>5</sup> CAEN N470 HV Power Supply, <http://www.caentechologies.com/csite/CaenProd.jsp?parent=21&idmod=238>

Considering a muon of energy in the order of GeV in interaction with an organic material  $Z \approx 6$ ,  $\rho \approx 1 \text{ g/cm}^3$ , it is in condition of M.I.P:

$$-\frac{dE}{dx} \approx 1.5 \frac{\text{MeV}}{\text{cm}}$$

Only a fraction of the total energy released [ $\Delta E \approx 1.5 \frac{\text{MeV}}{\text{cm}} \cdot 4\text{cm} = 6 \text{ MeV}$ ] excites molecular levels of the scintillating organic compound, which then rapidly de-excites  $O(ns)$  emitting UV photons. In a typical organic scintillator, visible photons [300 – 700 nm] are obtained by converting the primary light thanks to a wavelength shifter with a rate of  $1\gamma/100\text{eV}$ , obtaining  $\approx 60000\gamma\text{s}$ . Consider that our light collection system is such to allow that 25% [6] of them reach the photocathode. Here the conversion of the light into electrons, by means of photoelectric effect, has a  $<Q.E.> \approx 20\%$  [6] over the entire spectrum of collected photons. Thus the number of photoelectrons that reach the stage of multiplication in the tube are:  $N_e \approx 60000 \cdot 0.25 \cdot 0.2 = 3000$ . Assuming that the number of obtained electrons are Poisson distributed:

$$P(n, N_e) = \frac{(N_e)^n e^{-N_e}}{n!} \rightarrow P(0, N_e) = e^{-3000} \approx 0$$

Thanks to some simple approximation, our model 4 cm thick plastic scintillator has a intrinsic efficiency of 100% to detect M.I.P. particles. If we have a traditional PM tube with 10 stages and a dynode gain  $\delta \approx 4$  (note that the gain is strictly connected to the voltage supply  $\approx 10^3\text{V}$ ) and considering that the PM pulse travels in a cable with  $R = 50\Omega$  of impedance:

$$G \approx \delta^N = 4^{10} \rightarrow \Delta V \approx \frac{N_e \cdot e \cdot G}{\Delta t (\approx 100\text{ns})} \cdot R \approx 250 \text{ mV}, \Delta V(1e^-) \approx 0.084 \text{ mV}$$

This result is consistent with the amplitude of our PM output signals produced by the interaction between the muon and the detector, as shown in Fig.5.

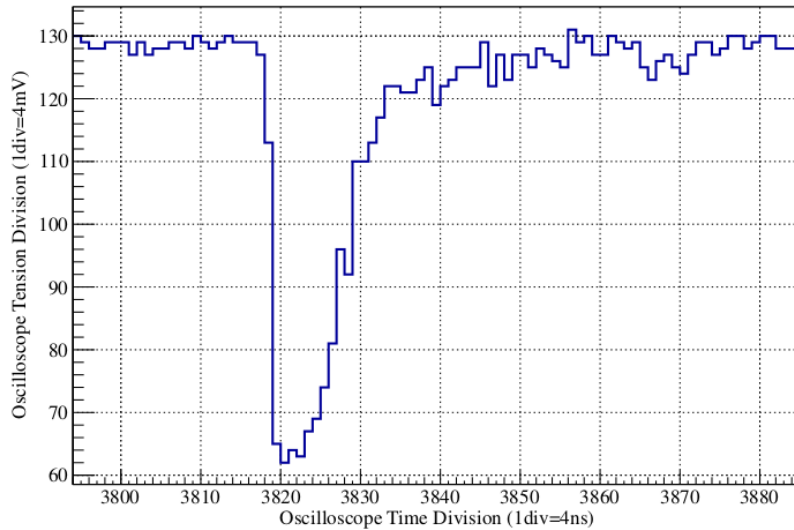


Figure 5: *Muon waveform taken from the oscilloscope.*

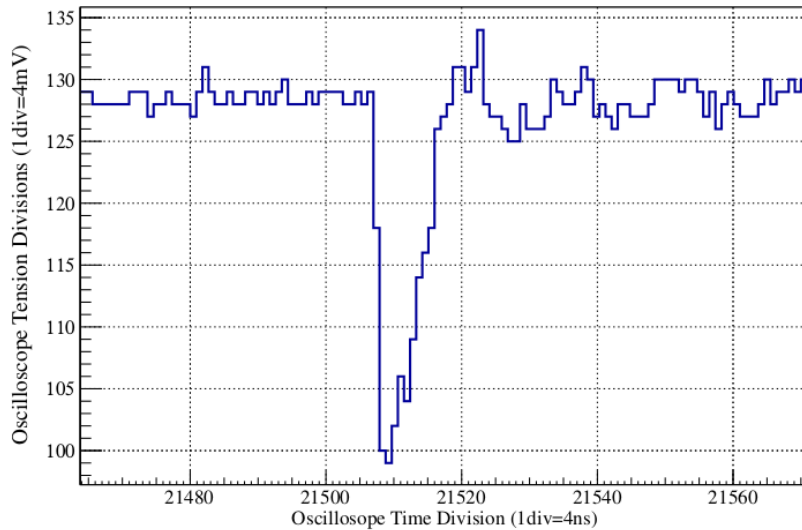


Figure 6: *Electron waveform taken from the oscilloscope.*

### 3 Scintillators Characterization

Before setting up the experimental apparatus, we characterize the three scintillators efficiency. Since whichever configuration for time measurement needs a trigger, we have also to study thresholds.

#### 3.1 Thresholds and Biases

Our goal consists of determining, for each scintillator, the working point and the trigger threshold in order to optimize scintillators efficiency. At first, for each scintillator the voltage is fixed at the value of 1KV. Then, we analyse the signal waveforms to choose a suitable threshold value. The waveforms have a maximum amplitude of  $V_{max} \approx 600\text{ mV}$  for SC1 (it stands for scintillator number one) and  $V_{max} \approx 350\text{ mV}$  for SC2 and SC3. Thus, the following thresholds are chosen: 220 mV → SC1 and 100 mV → SC2 and SC3. The efficiency measurement is based on counting muons crossing the different scintillators, using the configuration shown in Fig.7. The scintillators are put one upon the other, with spacings of 10 cm. After choosing the scintillator to analyse, we fix the other voltages and vary that scintillator bias. Our aim is to make double-coincidences and triple-coincidences using the electronic chain described in Fig.8. In this configuration the efficiency,  $\varepsilon$  is defined as:

$$\varepsilon(V) = \frac{N_{Triple}}{N_{Double}} \quad (11)$$

where  $N_{Double}$  is the number of double-coincidences between the bias-fixed scintillators and  $N_{Triple}$  is the number of coincidences among all of them. The width of the coincidence gate i.e. the width of the logic pulses produced by the discriminator is fixed to 100 ns. Note that with this method we don't need the bias-fixed scintillators to have 100% efficiency. For example, if we vary the SC1 bias:

$$N_{Double} = N_{TOT} \cdot \varepsilon_2 \cdot \varepsilon_3$$

$$N_{Triple} = N_{TOT} \cdot \varepsilon_1(V) \cdot \varepsilon_2 \cdot \varepsilon_3$$

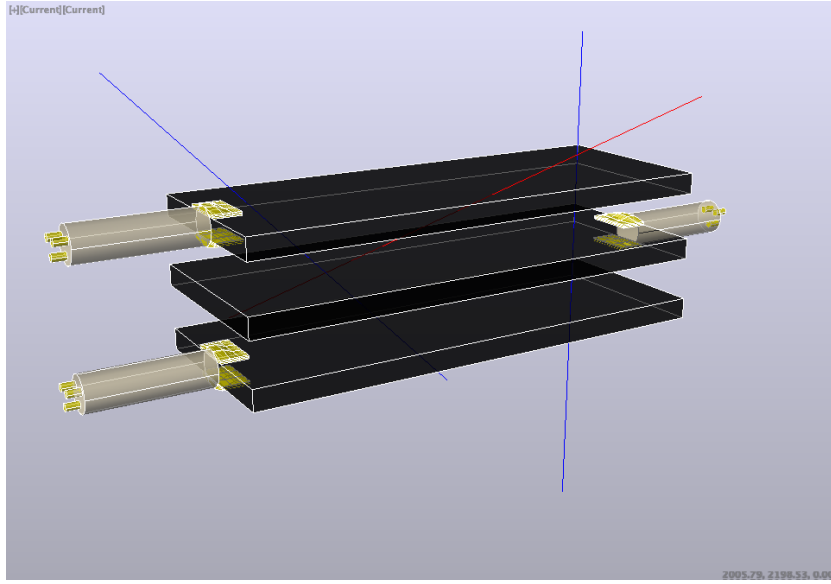


Figure 7: Efficiency measurement experimental setting.

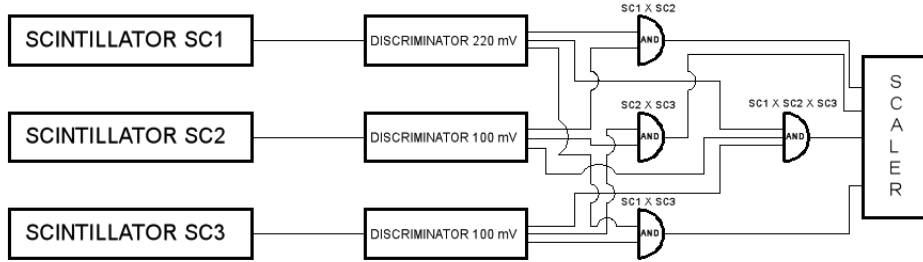


Figure 8: Electronic chain for efficiency measurements.

$$\varepsilon(V) = \frac{N_{Triple}}{N_{Double}} = \varepsilon_1(V) \quad (12)$$

It is expected that the function  $\varepsilon(V)$  has a steep raising and a plateau, at full capacity i.e. when  $\varepsilon \approx 100\%$ . It is also known the number of expected muons crossing the scintillators Eq.3, since their area is  $80.5 \times 30.3 \text{ cm}^2$  and we make 2 minutes long measures, the expected number of muons on the top scintillator is:

$$N_{Expected} = 4878 \pm 70$$

Because of this information, we analyse also the number of single counts varying voltages. We expect this to be a monotonic function with a plateau (at full capacity) and a steep raising for high voltages, caused by the excessive gain. Therefore, the best voltage has to be chosen not only evaluating the efficiency, but also the number of single counts we expect. Finally, having set each scintillator at the working point previously determined, we study efficiency and single counts varying the thresholds. The results are reported in Fig.9, 10 and 11 where the uncertainty on counts is taken as the Poissonian error  $\sqrt{N}$ . After analysing these graphs, the operating voltages and thresholds chosen are given in Tab.2. Note that only for the second scintillator the efficiency is 100%, this is probably because we have to take into account the uniformity of light

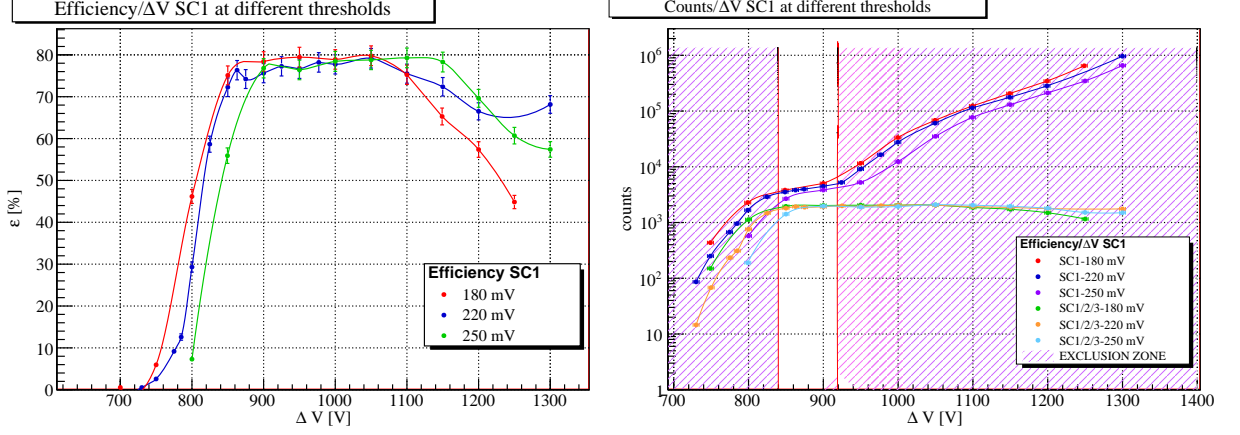


Figure 9: Left: SC1 efficiency  $\varepsilon$  vs  $\Delta V$  at different thresholds. Right: SC1 counts vs  $\Delta V$  at different thresholds.

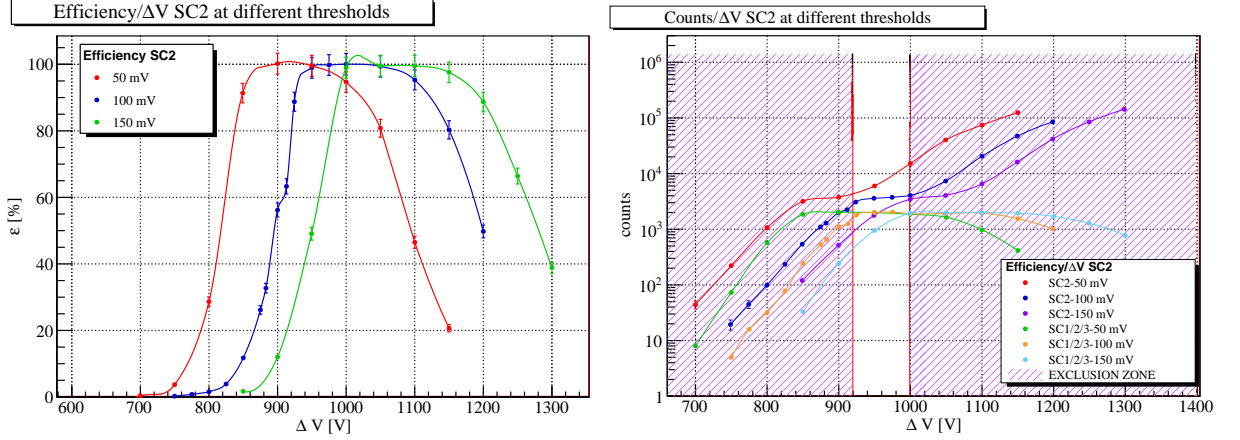


Figure 10: Left: SC2 efficiency  $\varepsilon$  vs  $\Delta V$  at different thresholds. Right: SC2 counts vs  $\Delta V$  at different thresholds.

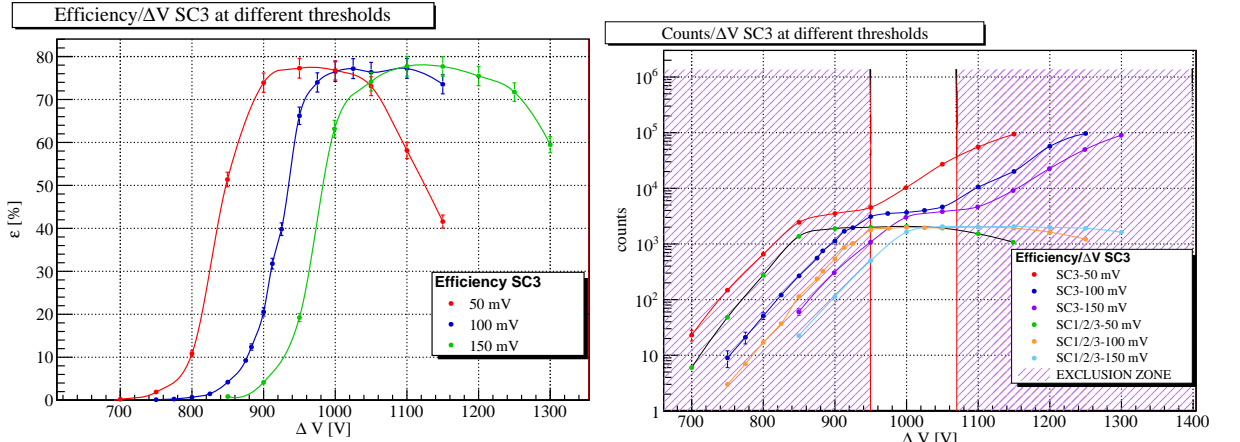


Figure 11: Left: SC3 efficiency  $\varepsilon$  vs  $\Delta V$  at different thresholds. Right: SC3 counts vs  $\Delta V$  at different thresholds.

yield and the geometrical efficiency as well.

| Scintillator | Threshold | Bias   | Efficiency [%]   |
|--------------|-----------|--------|------------------|
| SC1          | 220 mV    | 900 V  | $77.26 \pm 2.31$ |
| SC2          | 100 mV    | 975 V  | $99.79 \pm 3.12$ |
| SC3          | 100 mV    | 1025 V | $77.19 \pm 2.32$ |

Table 2: *Thresholds and biases*

### 3.2 Uniformity of Light Yield

The non-unitary efficiency of top and bottom scintillators, respectively SC1 and SC3, could be due to a high loss of light when it is produced far from PM. So, ideally, the light produced by a muon crossing the detector far away from the PM, may not be collected at the photocathode and leads to an unbalance between double and triple events. At first, SC1 and SC2 are exchanged, in order to cancel acceptance effects explained in the Sec.3.3. Then, in order to verify the existence of this effect, efficiency measurements are carried out inserting or extracting SC1 gradually from the experimental apparatus along the direction of phototube, as shown in Fig.12. It's

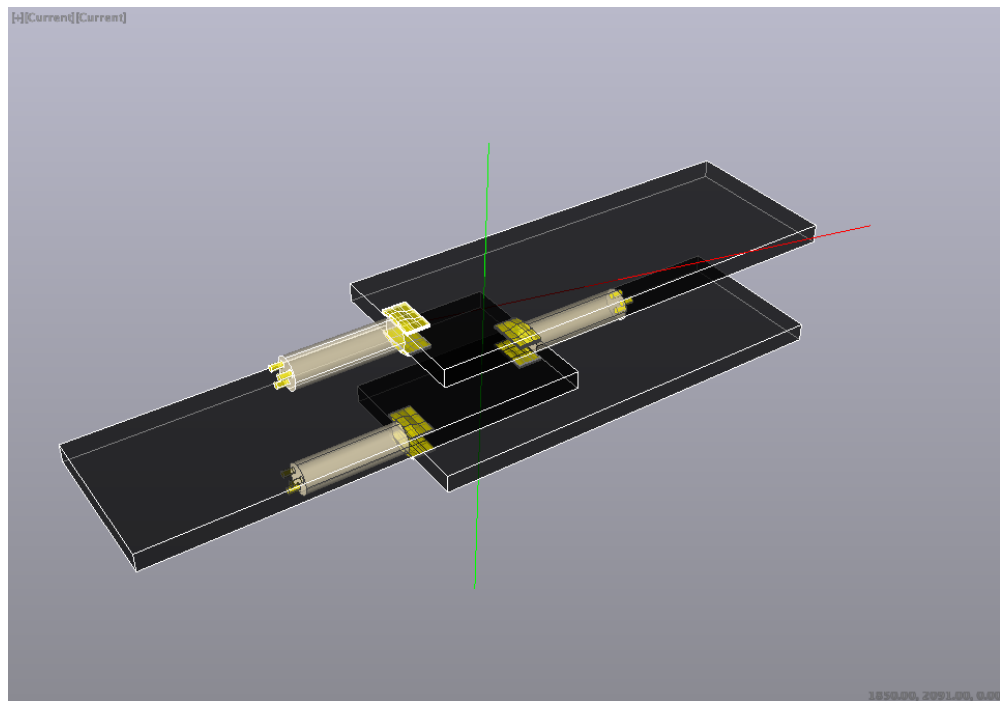


Figure 12: *Extraction of the central scintillator to prove the uniformity of light yield.*

easy to show how the trend of  $\varepsilon$  is linear respect to  $\Delta L$ , as reported in Fig.13. Considering the functional expression obtained from the linear fit, we can see how the efficiency vanishes when  $\Delta L \approx 80$  cm. Thus, the efficiency loss is only due to a proportional reduction of SC1 area available for coincidences.

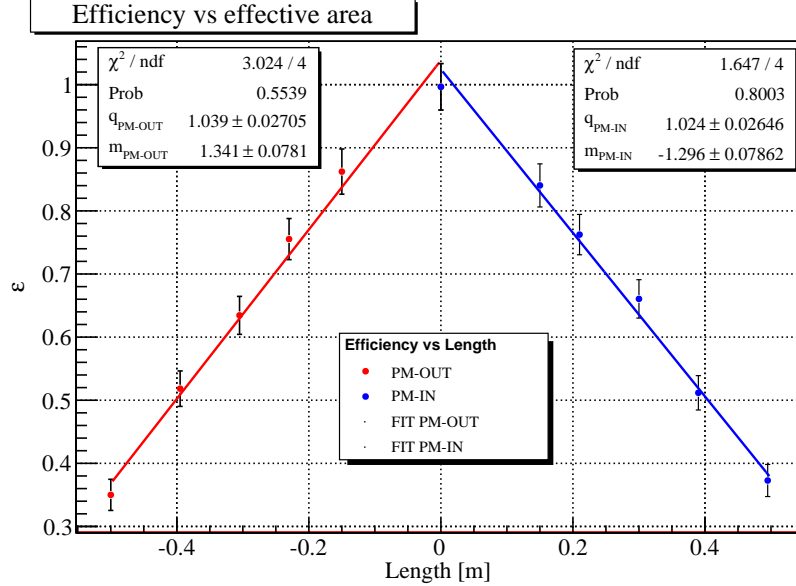


Figure 13: Trend of  $\varepsilon$  as function of  $\Delta L$ .  $\Delta L > 0 \rightarrow$  extract SC1,  $\Delta L < 0 \rightarrow$  insert SC1.

### 3.3 Monte-Carlo Simulation

A Monte-Carlo simulation has been developed to evaluate the geometric contribution to the efficiency of the experimental apparatus and to explain the non unitary efficiency, at full capacity, of SC1 and SC3<sup>6</sup>. In this simulation each event i.e. each muon generated is characterized by:

- The two coordinate ( $x;y$ ) of the application point on SC1 are generated according to an uniform distribution  $x \in [0, 80.5]$  and  $y \in [0, 30.3]$ .
- The used uniform pseudo-random number generator belongs to the **TRandom3** class of ROOT package [7]. It is based on the "Mersenne Twister generator", it is fast  $45 \frac{ns}{call}$  and it has a large period  $10^{6000}$ .
- The direction of the muon is described by two angles: the azimuthal one is uniformly distributed between  $[-\pi; \pi]$ , while the polar angle follows the distribution shown in Eq.4. The area  $dA$  should be considered to have its normal along the incoming direction of the muon. So, as shown in Fig.14, it must be projected on the scintillator through the equation:

$$dA' = dA \cos \theta \rightarrow \frac{dN}{dA' d\Omega dt} = \frac{d\Phi_{flux}}{d\Omega} \approx I_0 \cos^3 \theta$$

$$\frac{d\Phi}{d\theta} \sim \cos^3 \theta \sin \theta = f(\theta) \quad (13)$$

<sup>6</sup>We have simulated the geometric efficiency of the lower scintillator which is equal, by symmetry, to that of the upper.

Eq.13 establishes the polar angular distribution of the muon flux on SC1. The generation of  $\theta$  in the Monte-Carlo is performed through the hit/miss method of Von Neumann.

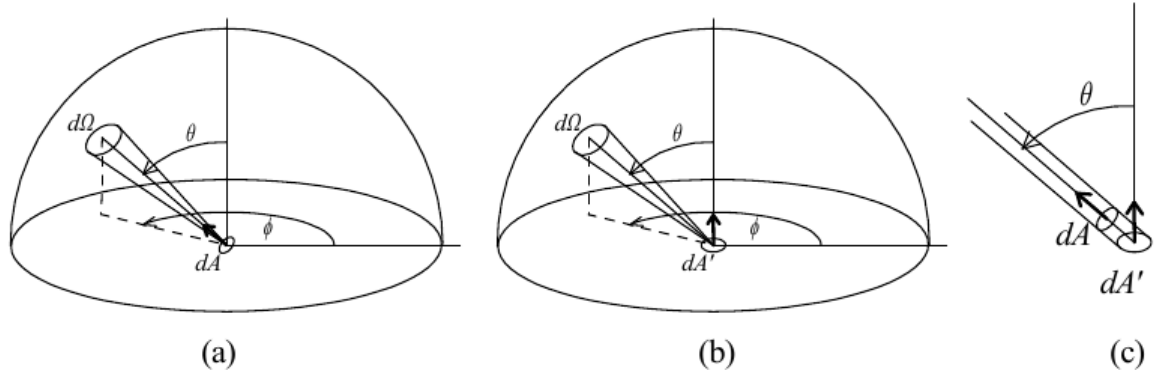


Figure 14: In (a) the area element is oriented in the direction of incoming muon. In (b) the area element is oriented vertically, (c) shows equivalent areas for the two cases:  $dA' = dA \cos \theta$ .

The Von Neumann method is commonly used when we want to generate events according to a generic pdf. In this case two numbers are uniformly generated: a polar angle  $\theta_i$  between  $[-\frac{\pi}{2}; \frac{\pi}{2}]$  and a weight  $f_0(\theta)$  between  $[min\{f(\theta)\}; max\{f(\theta)\}] \Rightarrow [0, \frac{3\sqrt{3}}{16}]$ . Only if  $f(\theta_i) < f_0(\theta)$  the event is accepted. After that, muon geometrical coordinates on the other two scintillators  $[(x'; y'), (x''; y'')]$  are calculated thanks to:

$$\begin{aligned} x' &= x + r' \sin \theta \cos \phi \rightarrow r' = \frac{h}{\cos \theta} & x'' &= x + r'' \sin \theta \cos \phi \rightarrow r'' = \frac{2h}{\cos \theta} \\ y' &= y + r' \sin \theta \sin \phi & y'' &= y + r'' \sin \theta \sin \phi \end{aligned}$$

where  $h$  is the distance between the SC1 and SC2. If  $x' \in [0, 80.5]$  and  $y' \in [0, 30.3]$  the muon crosses the second scintillator, so we have a double count, whereas if  $x'' \in [0, 80.5]$  and  $y'' \in [0, 30.3]$  we have a good triple count. As already said, the geometric efficiency is the ratio:

$$\varepsilon_g = \frac{N_{\text{triple}}}{N_{\text{double}}}$$

Five hundred independent simulations have been developed, each one with 25000 muons, every time changing the uniform generator seed.<sup>7</sup> In Fig.15, 16 and 17 are reported the spatial distributions of all generated muons on the three scintillators after the selections previously described. The distribution of geometric efficiency, evaluated in each simulation, is shown in Fig.18. This is fitted with a Gaussian pdf dependent on three parameters:

$$g(\varepsilon_g; \hat{A}, \hat{\varepsilon}_g, \hat{\sigma}_g^2) = \hat{A} \cdot e^{-(\varepsilon_g - \hat{\varepsilon}_g)^2 / (2\hat{\sigma}_g^2)}$$

that are estimated through a binned  $\chi^2$  method given the following result:

|                                  |                            |
|----------------------------------|----------------------------|
| $\hat{\varepsilon}_g = 0.771656$ | $\hat{\sigma}_g = 0.00013$ |
|----------------------------------|----------------------------|

$$\chi_0^2 = \frac{\chi^2}{n_{df}} = \frac{111.6}{102} \quad P(\chi^2 \geq \chi_0^2) = 24.17\% \in 95\% C.L$$

This simulated value for geometric efficiency  $\hat{\varepsilon}_g$  is consistent with the two experimental values obtained, as shown in Tab.2, for SC1 and SC2. So it has been shown how the deficit of efficiency is caused only by geometrical effects.

<sup>7</sup>The seed is set using a 128 bit UUID. This results in different seeds and random sequence for every call.

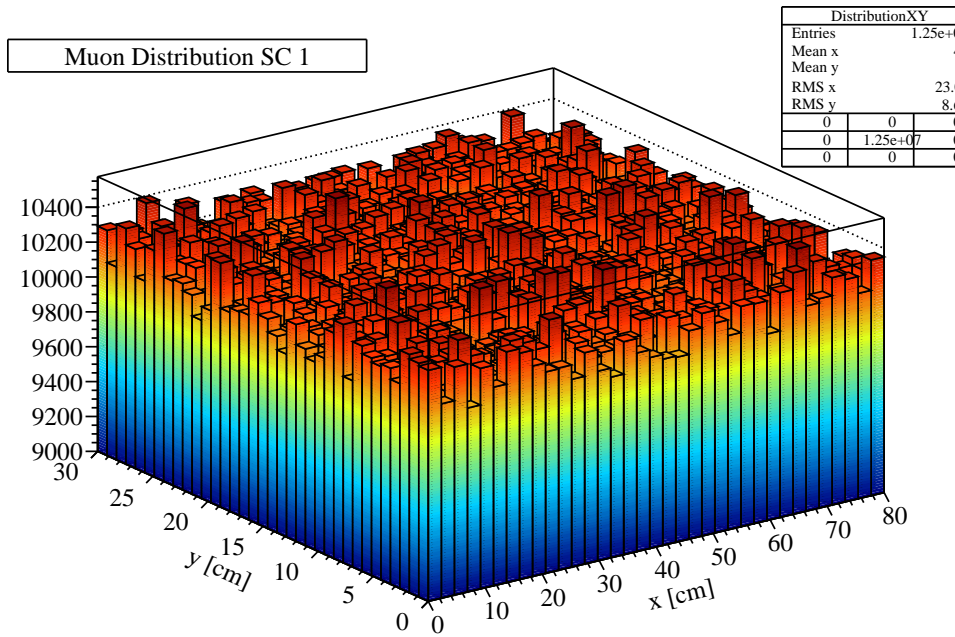


Figure 15: *Muons generated on the top scintillator.*

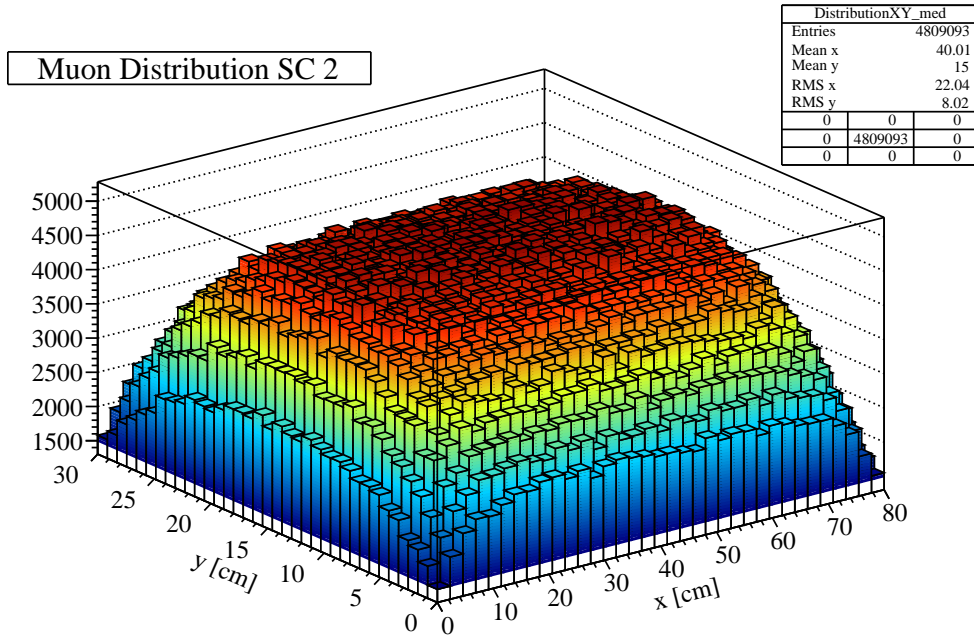


Figure 16: *Muons crossing the middle scintillator.*

## 4 Lifetime Measurements

In this section we describe how to perform  $\mu$  lifetime measurements in different absorbers. The electronic chain used for the signal processing is shown in Fig.19. The scintillators SC1, SC2 and SC3 are supplied by the voltages reported in Tab.2. The anodic output signals enter the discriminator where the thresholds are fixed to values previously chosen, see Tab.2. For SC2

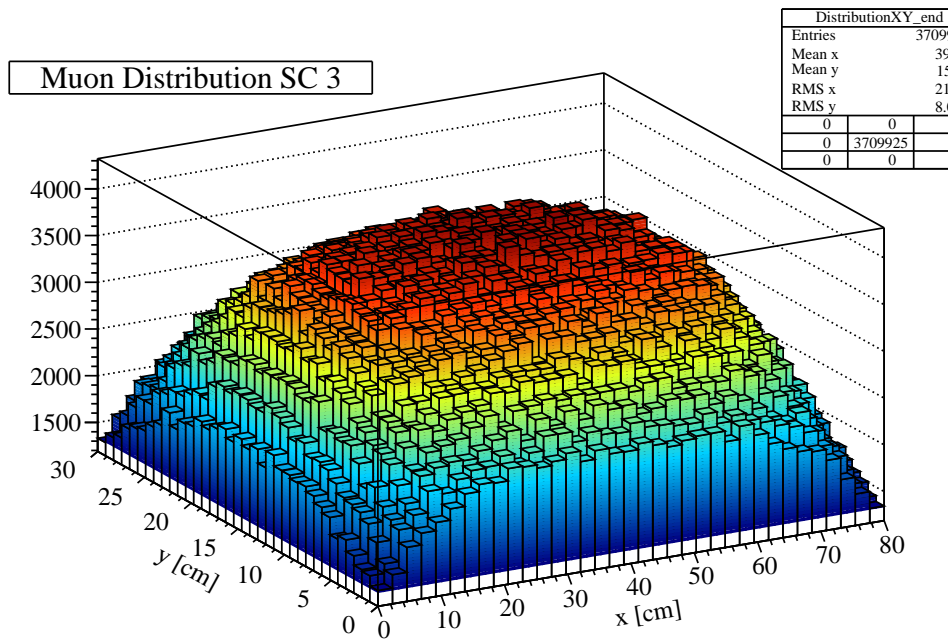
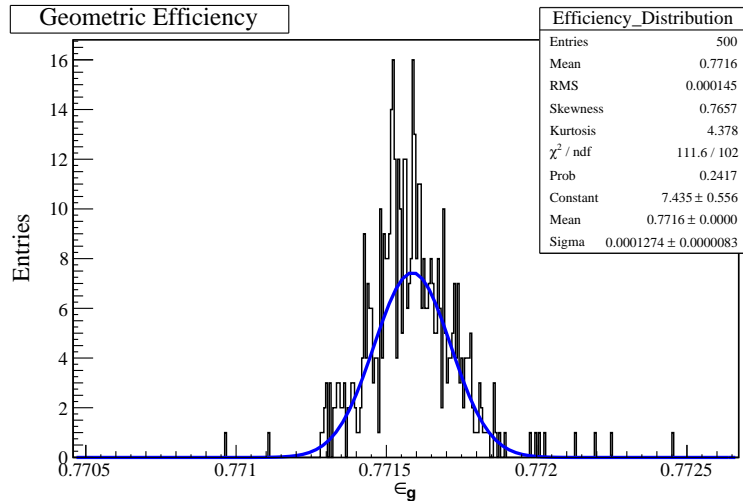


Figure 17: Muons crossing the lower scintillator.

Figure 18: Distribution of  $\epsilon_g = \frac{N_{\text{triple}}}{N_{\text{double}}}$ .

and SC3, before entering the trigger unit, the outputs are split so that they can also be taken to the oscilloscope (SC2→CH1, SC3→CH2). The rest of the electronic chain is used to form the trigger signal given to the oscilloscope. It consists of the following steps:

1. The discriminator outputs enter a Fan-In/Fan-out so that they can be multiplied.
2. Signals arrive to the 4-fold programmable logic unit with veto. The aim is to perform start and stop topology for the muon decay triggering. The start consists of a muon crossing SC1 and SC2 without a SC3 signal (the topology is  $SC1 \times SC2 \times \overline{SC3}$ ). This doesn't guarantee that this is a muon decay. In fact, there is also the possibility for the muon to cross SC1 and SC2 without SC3 signal because of geometric acceptance. So, we need

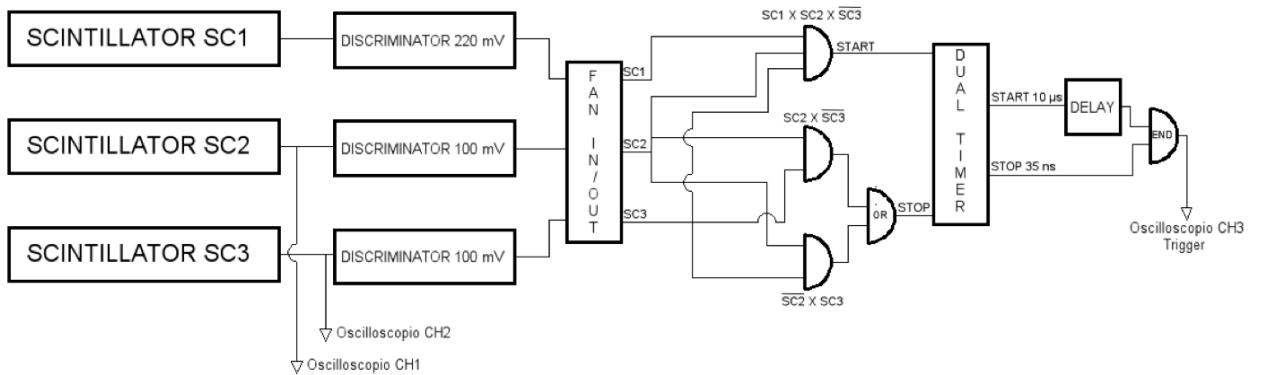


Figure 19: *Electronic chain used for muon lifetime measurement.*

another constraint, called stop signal, given by  $SC2 \times \overline{SC3}$  or  $SC3 \times \overline{SC2}$ .

3. The logic-or is realized by a quad coincidence unit. At this time, the ultimate goal is to form the trigger signal through a coincidence between start and stop.
4. The start is widened up to  $10 \mu s \approx 5 \tau^+$ , thus the apparatus is susceptible to time measurements in the range  $[0, 10] \mu s$ .
5. Note that all start events are included in the stop topology  $SC2 \times \overline{SC3}$ , so each start gives also a stop. Because of this the start is delayed through an octal gate and delay generator.
6. Finally, the trigger signal is formed by the coincidence between start and stop and sent as external trigger to the oscilloscope.

## 4.1 Coincidence Characterization

One of the most important coincidence measure aspect is the gate width. *A priori*, we would want a as narrow as possible gate in order to have the best time resolution. On the other hand, if the resolution is too narrow, signals fluctuations on the time scale can take out-of-coincidence simultaneous signals. The characterization is performed only using SC1 and SC2; at first we take the scintillators signals into a delay generator and delay one of them. Secondly, the outputs enter the coincidence unit. Finally the signal is taken to a scaler in order to make a coincidence counts measurement, as shown in Fig 20. The measurement consists of fixing the coincidence gate, varying the outputs relative delay and measuring the counts. The result is the coincidence spectrum which is expected to be: symmetric, with a plateau for small delay and constant background for long delay, due to random coincidence. The best gate width choice is based on an evident plateau and a symmetric profile. Knowing each scintillator free rate ( $R_1 = 32$  Hz,  $R_2 = 36$  Hz), random coincidence rate is given by:

$$R_{casual} = 2 \cdot \tau \cdot R_1 \cdot R_2 \quad (14)$$

where  $\tau$  is the coincidence gate. If  $\tau \approx 100$  ns,  $R_{casual} \approx 2 \times 10^{-4}$  Hz. The resulting spectra are shown in Fig. 21, 22. As we can see, the best choice is  $\tau = 50$  ns. Now on, we set whole logical pulses width at 50 ns, except for start that is widened to 10  $\mu s$ .

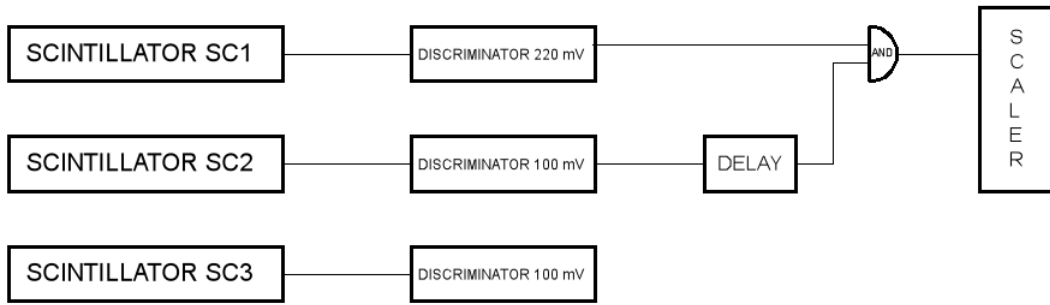


Figure 20: *Electronic chain for coincidence characterization.*

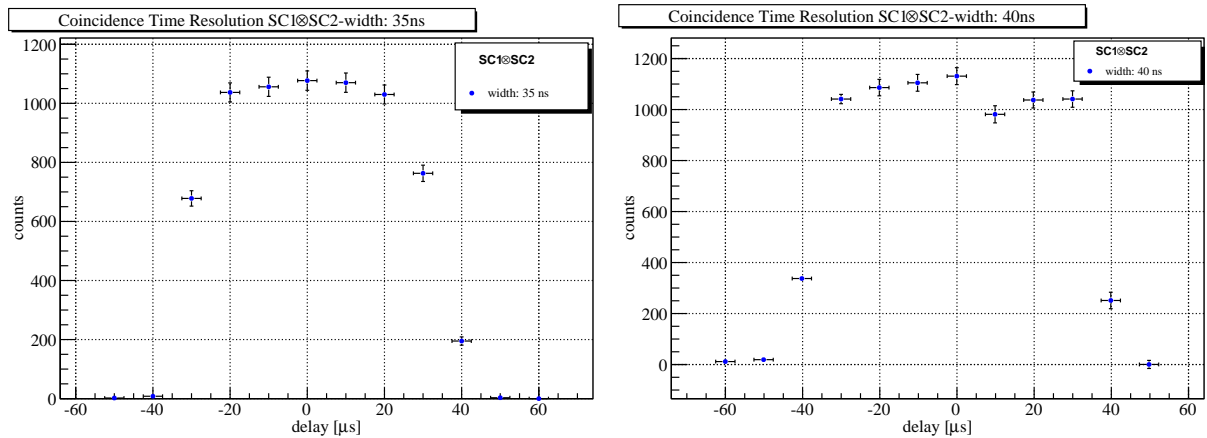


Figure 21: *Left: Coincidence Time Resolution for gate 35 ns. Right: Coincidence Time Resolution for gate 40 ns.*

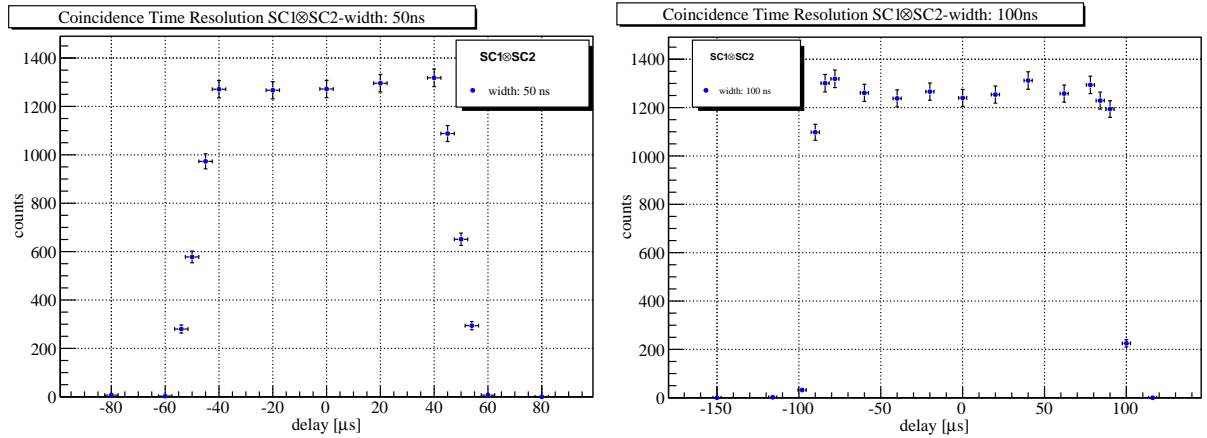


Figure 22: *Left: Coincidence Time Resolution for gate 50 ns. Right: Coincidence Time Resolution for gate 100 ns.*

## 4.2 Start-Stop Delay

With the aforementioned apparatus, each start signal guarantees also one of the stop topology. In order to solve this problem we delay the start from the stop, thus they become out-of-

coincidence. Our aim is to choose the delay so that it suppresses the possibility of start-stop simultaneous coincidence, due to time-jitter. For whichever chosen delay, we lose some true decay events, so the optimal delay balances the two effects. The optimal choice is performed by varying start-stop delay and counting the coincidence events. We expect the events distribution to be a step-function with the leap when the time-jitter lets start signal coincides with stop one. We also reduce gate width of start events to verify the decreasing of counts, as expected. As shown in Fig.23, the optimal delay is 60 ns, note that start-stop delay begins from stop rising and ends at start rising.

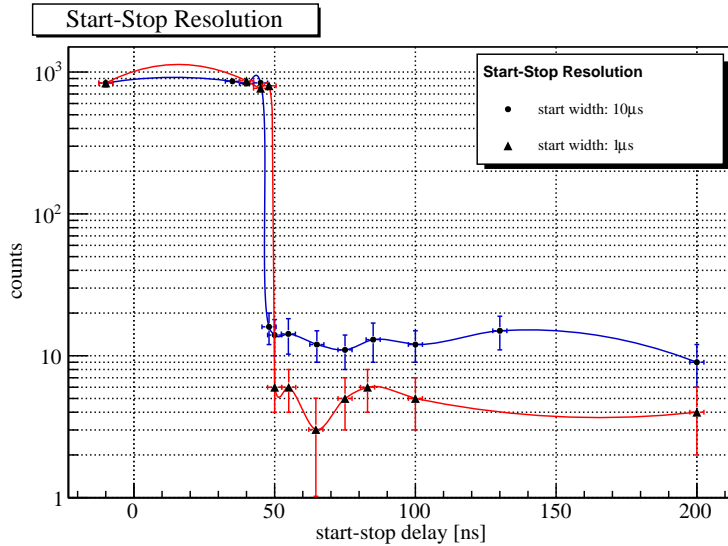


Figure 23: *Coincidence counts varying start-stop delay.*

### 4.3 Waveform Analysis Software

The developed logic and the used electronic, as described in Sec.4, allow to have a trigger for muon decay events. If there is a coincidence between a start  $SC1 \times SC2 \times \overline{SC3}$  and a stop  $SC2 \times \overline{SC3}$  or  $SC3 \times \overline{SC2}$ , in a gate of  $10\mu s$ , a logic signal is sent as external trigger to the oscilloscope. In free or bound muon lifetime measurement, the oscilloscope inputs are the scintillators  $SC2 \rightarrow CH1$  and  $SC3 \rightarrow CH2$ . When a trigger event is present, the software acquires the complete waveform on CH1 and CH2. The software implementation can be found in the Appendix B. At first, the software selects some basic settings:

- The time scale is set in units of  $\mu s$ /div, on a range of  $10\mu s$ . The trigger event is fixed with an offset of  $-4\mu s$  respect to the middle of the time axis. In this way, it is susceptible to decay times  $\in [0, 9]\mu s$ .
- The vertical voltage scale is set in units of mV/div.
- The trigger source is set to external, mode edge slope fall (trigger on the signal slope fall).
- The data transfer is set in binary encoding, in order to make it faster.
- The waveform is sampled at 2500 points, i.e. with a time resolution of 4 ns.

Then, the system is ready to acquire the signals according to a trigger event. When this occurs, it looks first for the start signal on CH1. A loop iterates from the beginning of the waveform till

it falls below a threshold level, that is the same sets in the discriminator<sup>8</sup>. At this moment, the point position  $t_i$  and its amplitude are stored. After that, a simple procedure is implemented to assess the maximum amplitude and to control the shape of the signal. Starting a loop from  $t_i$  up to  $t_i + 68$  ns (17 *div*), it updates the signal amplitude and requires that, within this range, the signal goes back above the trigger level<sup>9</sup>. If this condition is met, the start event is accepted. This criterion is derived analysing, with the oscilloscope, the signals characteristics (maximum amplitude  $\in [300, 600]$  mV, temporal extension  $\in [100, 120]$  ns). Thanks to these controls, we can exclude signals with strange shape due, for example, to noise, to rise pile-up or tail pile-up. A limitation of this procedure is that it is purely qualitative, so it does not give a complete rejection of the pile-up. Indeed, if there is a tail pile-up above the threshold, it will not be subject to rejection. However, since the probability of observing one or more pile-up events on start and stop signals is very small, the development of an algorithm for the complete rejection of the pile-up is superfluous. A similar procedure is applied in the study and in the research of stop signals. Here there are two possible topologies, due to an electron revealed by SC2 or by SC3. Differently from what has been done for the start signal, we know that the stop, on CH1 or CH2, is placed close to 9  $\mu$ s. Analyzing in a range of 120 ns around the trigger position, the previous algorithm is implemented in order to establish the time position  $t_f$  of the stop event. In a normal decay event it is expected only one start and only one stop but, just from the observation of the first free decays, we have observed other possible topologies:

- **Double start and one stop:** when there is a signal on CH2 in the same range time of the start, which is always placed on CH1.
- **Double stop and one start:** when there is a stop signal both on CH1 and CH2.
- **Double start and double stop.**

So, we have added in the DAQ software an algorithm in order to recognize these type of events. For example, if we consider the dataset related to the decay of free muon we have:  $N_{tot} = 8211$ ,  $D_{start} = 691 \rightarrow \approx 8\%$  and  $D_{stop} = 79 \rightarrow \approx 1\%$ . Double stop events are probably due to a muon decayed in the scintillator SC2 and not in the space between SC2 and SC3, with an electron emitted and detected by SC3. However, in our further analysis double start an stop events are discarded. Finally the DAQ software calculates the time interval  $\Delta t$  between start and stop converting the value in  $\mu$ s and adding the start/stop delay  $\Delta t_{delay} = 60$  ns.

## 4.4 Data Analysis

The muon decay is a completely random event that does not depend on the past history of the particle. Thus, the probability  $dP$  of decay in the next infinitesimal time interval  $dt$  is independent of how long it has lived since production and is given by:  $dP = \Gamma dt$ . Taken a sample of N particles, the number of them which disappear from the sample due to the decay in  $dt$ , are:

$$-dN = N \cdot dP = N \cdot \Gamma dt \quad \xrightarrow{N(t_0)=N_0} \quad N(t) = N_0 e^{-\Gamma(t-t_0)} \quad (15)$$

In an experiment of lifetime measure, where is not possible to distinguish free from bound decays, the time distribution of the reconstructed decay events has the following general form:

$$f(t; B, A^+, A^-, \tau^+, \tau^-) = B + \frac{A^+}{\tau^+} e^{-t/\tau^+} + \frac{A^-}{\tau^-} e^{-t/\tau^-} \quad (16)$$

<sup>8</sup> Signals from the scintillators have negative polarity because they are formed at the anode.

<sup>9</sup>This temporal range is the same of the logic signals produced by the discriminator.

where  $\tau^+$  and  $A^+$  are related to the free decays contribution,  $A^-$  and  $\tau^-$ , instead, characterize the bound decays spectrum. Finally B is related to background events due to random coincidences between a start and a stop signal in the measurement gate of  $10\ \mu s$ . Considering a sample of N events  $\{t_i\}$ , in the assumption that they are distributed according to Eq.16, we can estimate the lifetimes and the amplitudes through a fit of the experimental distribution of the measured  $\{t_i\}$ . In each fit performed, the background is fixed according to the rate of random coincidences foreseen, given by:

$$R_{Casual} = 2R_{Start} \cdot R_{Stop} \cdot \Delta t_{Gate} \rightarrow N_{Back} = R_{Casual} \cdot T_{Measure} \quad (17)$$

where  $\Delta t_{Gate} = 10\ \mu s$ ,  $T_{Measure}$  is the time needed to collect the sample  $\{t_i\}$  while  $R_{Start} = 4.55\text{ Hz}$  and  $R_{Stop} = 21.94\text{ Hz}$  are the single rate for start and stop evaluated by counting these events in a  $\Delta t_{Rate} = 30000\text{ s}$ . With these values the  $R_{casual} \approx 2 \cdot 10^{-3}\text{ Hz}$ . Finally, assuming that  $N_{Back}$  are uniformly spread on the time scale, the number expected in each bin is:

$$B = 2R_{Start} \cdot R_{Stop} \cdot \Delta t_{bin} \cdot T_{Measure} \quad (18)$$

The conspicuous difference between  $R_{Start}$  and  $R_{Stop}$  is due to:

- Start events,  $SC1 \times SC2 \times \overline{SC3}$ , are muons that don't cross SC3 for geometrical reasons or decay between SC3 and SC2 (or in SC2). Therefore, their rate can be considered stable in time.
- Stop events,  $SC2 \times \overline{SC3}$  or  $SC3 \times \overline{SC2}$ , are particles passing only one scintillator or they can be produced by electronic noise such as gain fluctuations of PMs, changing of supply voltages, threshold fluctuations. For this reasons, in order to have an accurate estimation of  $R_{Stop}$ , we measured the rate for  $\Delta t_{rate} = 30000\text{ s} \approx 8\text{ h}$ .

The experimental data  $\{t_i\}$  are put into histograms with a bin width equal to the waveform sampling resolution made by the oscilloscope (4 ns). So, the time axis is divided into 2500 bins in the range  $[0, 9]\ \mu s$ , as already exposed in Sec.4.3.

#### 4.4.1 Measure of Free Lifetime

The measure of free lifetime has been carried out via two different experimental configurations:

1. The gap between SC2 and SC3 is left empty so, in the decay time distribution we have two exponential terms:

$$f(t; B, A^+, A^-, \tau^+, \tau^-) = B + \frac{A^+}{\tau^+} e^{-t/\tau^+} + \frac{A^-}{\tau^-} e^{-t/\tau^-}$$

where  $\tau^-$  stands for the  $\mu^-$  lifetime in the scintillator SC2 ( $(2CH_3)C_6H_4CHCH_2$  Polyvinyl-Toluene) that can be considered, in good approximation, as if it were made of carbon (C,Z=6). Since our experimental apparatus is not sensitive to capture decays, the integrals of  $\mu^+$  and  $\mu^-$  distribution can be correlated by:

$$\frac{A^+}{A^-} = \frac{N_\mu^+/N_\mu^-}{N_\mu^-/N_\mu^+} = \frac{f_\mu^+}{f_\mu^-}$$

where, as shown in Fig.2, we can put  $f_\mu^+ \approx 0.56$  and  $f_\mu^- \approx 0.44$ . We obtain:

$$A^- = \frac{A^+ f_\mu^-}{f_\mu^+} \quad (19)$$

Thus, the time distribution in Eq.16 becomes:

$$f(t; B, A^+, A^-, \tau^+, \tau^-) = B + \frac{A^+}{\tau^+} e^{-t/\tau^+} + \frac{A^-}{\tau^-} e^{-t/\tau^-} = B + \frac{A^+}{\tau^+} (e^{-t/\tau^+} + \frac{f_\mu^- \tau^+}{f_\mu^+ \tau^-} e^{-t/\tau^-})$$

if we consider  $\tau^+ \approx \tau^-$ :

$$f(t; B, A^+, A^-, \tau^+, \tau^-) = B + \tilde{A} \cdot (f_\mu^+ e^{t/\tau^+} + f_\mu^- e^{-t/\tau^+}) \quad (20)$$

This is the hypothesis on the data pdf that we use in the fit procedure.

2. The gap between SC2 and SC3 is filled with an high Z absorber, in our case with lead (Pb, Z=92). In this way, the probability of  $\mu^-$  decay in the nucleus becomes large therefore  $\tau^-$  short in fact  $\tau^-(Pb) \approx 75$  ns, as reported in Tab.1. Thus, taking the general distribution of decay events in Eq.16, we can do the following approximation:

$$f(t; B, A^+, A^-, \tau^+, \tau^-) \xrightarrow{t \gg \tau^-} f'(t; B, A^+, \tau^+) = B + \frac{A^+}{\tau^+} e^{-t/\tau^+} \quad (21)$$

In this approximation the exponential contribution of muons decayed in the scintillator is neglected.

In both configurations, the parameters estimation from the experimental sample  $\{t_i\}$  is carried out through a binned maximum likelihood method (BML). Considering the time measurements  $\{t_i\}, i = 1, \dots, n_{tot}$  as independent events, under the assumption that they are distributed according to a pdf  $f(t_i, \vec{\theta})$  dependent on  $m$  parameters  $\vec{\theta} = (\theta_1, \dots, \theta_m)$ , the joint probability of observing  $t_i$  in the interval  $(t_i, t_i + dt_i) \forall i$  is given by:

$$P(\{t_i\}) = \prod_i f(t_i, \vec{\theta}) dt_i \rightarrow L(\vec{\theta}) = \prod_i f(t_i, \vec{\theta})$$

where  $L(\vec{\theta})$  is called unbinned likelihood function. If we subdivide the data into  $N$  bins each one with  $n_j$  entries,  $n_{tot} = \sum_j^n n_j$ , the expected value of entries  $\nu_j$  in each bin is given by (provided that  $\int_{t_{min}}^{t_{max}} f(t, \vec{\theta}) dt = 1$ ):

$$\nu_j(\vec{\theta}) = n_{tot} \int_{t_j^{min}}^{t_j^{max}} f(t, \vec{\theta}) dt$$

The binned likelihood, in our case, is built assuming a Poisson probability density function for each entries  $n_j$  without bin-bin correlation:

$$L(\vec{\theta}) = \prod_{j=1}^N \frac{\nu_j^{n_j} e^{-\nu_j}}{n_j} \quad (22)$$

The best estimation of the parameters  $\vec{\theta}$  is obtained by maximizing  $L(\vec{\theta})$  or, easily:

$$\ln(L(\vec{\theta})) = \sum_{j=1}^N \left[ n_j \ln(\nu_j(\vec{\theta})) - \nu_j(\vec{\theta}) - \ln(n_j) \right] \quad (23)$$

This is quite different from the  $\chi^2$  method where, assuming a Gaussian pdf for each bin  $j$ , the  $\ln(L(\vec{\theta}))$  has the form:

$$\ln(L(\vec{\theta})) = -\frac{1}{2} \sum_{j=1}^N \frac{(n_j - \nu_j(\vec{\theta}))^2}{\sigma_j^2} \rightarrow \chi^2(\vec{\theta}) = \sum_{j=1}^N \frac{(n_j - \nu_j(\vec{\theta}))^2}{\sigma_j^2} \quad (24)$$

In this case, the best estimation of  $\vec{\theta}$  follows from the minimization of  $\chi^2$ . We choose to use the first method, described by Eq.23, because having set a short binning of 4 ns, it has the advantage of treating correctly the empty bins and use them in the fit procedure. Instead, a proper use of  $\chi^2$  method requires to skip the empty bins, therefore they are not considered in the fit.<sup>10</sup> The minimization is performed through **TMinuit** class of ROOT Package, the algorithm used is **MIGrad** that is based on conjugate directions method, in particular it is a stable variation of Davidon-Fletcher-Powell algorithm. The method MIGrad implemented in TMinuit, when it is used in the default mode, evaluates the minimum of an input parametric function with a stopping precision of  $10^{-6} \cdot \sum_j \sigma_j^2$ . MIGrad calculates also the error matrix through finite differences in the parabolic approximation. Finally, **MINOs** method evaluates more precisely the parameters errors taking into account correlation and non-parabolic effects [8].

The sample data collected in the Config.1, with  $n_{tot} = 8211$  decay events, is shown in Fig.24. The likelihood fit is performed in the time interval  $[0.65, 8.7]\mu s$ , using the pdf shown in Eq.20, where  $B$  and  $\tau^-$  are fixed as the values:  $B$  according to Eq.18 while  $\tau^- = 2.025\mu s$  as listed in Tab.1. Thus, there are only two free parameters:  $\hat{A}$  and  $\tau^+$ . The fit leads to the following

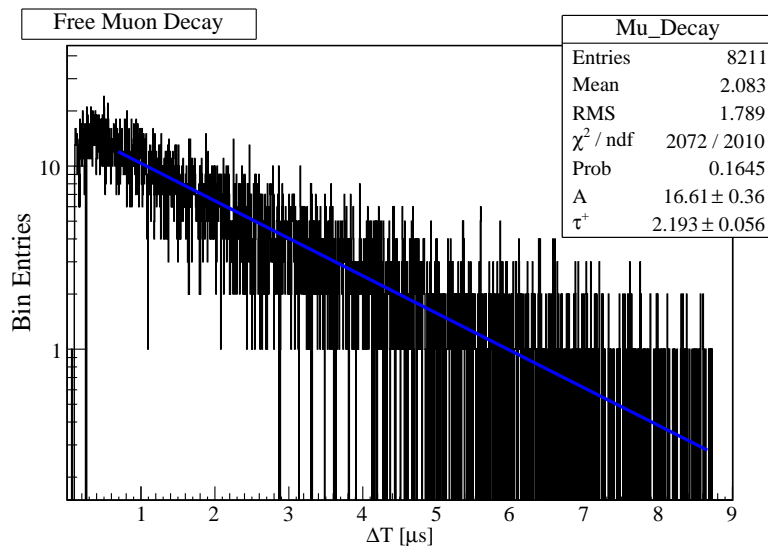


Figure 24: Fit of free muon decay events in Config.1.

parameters values and errors:

$$\hat{A} = 16.61 \quad \hat{\sigma}_{\hat{A}} = 0.36 \quad \hat{\tau}^+ = 2.193 \mu s \quad \hat{\sigma}_{\tau^+} = 0.056 \mu s \quad (25)$$

In addition, the errors and the correlation matrix are:

$$V = \begin{pmatrix} \hat{\sigma}_{\hat{A}}^2 = 0.13 & \hat{\sigma}_{A\tau^+} = -0.017 \\ \hat{\sigma}_{\tau^+ A} = -0.017 & \hat{\sigma}_{\tau^+}^2 = 0.0031 \end{pmatrix} \quad \rho = \begin{pmatrix} \hat{\rho}_{\hat{A}\hat{A}} = 1 & \hat{\rho}_{\hat{A}\tau^+} = -0.82 \\ \hat{\rho}_{\tau^+ A} = -0.82 & \hat{\rho}_{\tau^+\tau^+} = 1 \end{pmatrix}$$

So, observing the correlation matrix off-diagonal elements,  $\tau^+$  and  $\hat{A}$  are anti-correlated. This is due to the fact that if the amplitude of an exponential is reduced, maintaining fixed its compact support, its fall becomes less steep i.e.  $\tau^+$  increases. The  $\chi^2$  value returned by Minuit is calculated according to its definition, reported in Eq.27, where  $\nu_j(\vec{\theta})$  is evaluated for each bin

<sup>10</sup>The log-likelihood function is constructed from data thanks to the "L" option of the fit method for the **TH1** ROOT Package Class: <http://root.cern.ch/root/html/TH1.html#TH1>.

(the empty bins are not skipped) after the minimization process and  $\sigma_j^2 = \nu_j(\vec{\theta})$ . The  $\chi^2$  value and its probability, obtained from the fit, are:

$$\boxed{\chi_0^2 = \frac{\chi^2}{n_{df}} = 1.031} \quad P(\tilde{\chi}^2 \geq \chi_0^2) = 16.45\% \in 95\% C.L.$$

However, these results cannot be considered completely reliable, in fact:

- When we consider a sample of a random variable  $\{x_i\}$ , distributed according to the pdf  $f(x, \theta)$ , the maximum likelihood method allows to estimate  $\theta$  as  $\hat{\theta}$ . The estimator  $\hat{\theta}$  is itself a random variable, dependent from  $\{x_i\}$ , distributed according to  $g(\hat{\theta}, \theta_{true})$ . In general terms, ML estimators are consistent, not biased or asymptotically not biased, robust and  $g(\hat{\theta}, \theta_{true})$  is approximately Gaussian [9]. The problem is that  $g(\hat{\theta}, \theta_{true})$  is not known, so if we want a correct estimate for the variance  $\hat{\sigma}_{\hat{\theta}}^2$  we have to build  $g(\hat{\theta}, \theta_{true})$  from a Monte-Carlo simulation.
- The  $\chi^2$  is a measurement of the global agreement between the data and the hypothesis made about their distribution. In fact, if  $n_j$  are independent Gaussian variables, and if the functional hypothesis for  $\nu_j(\vec{\theta})$  is true, the  $\chi^2$  value, obtained from the minimization of Eq.27, is distributed according to the  $\chi^2$  distribution:

$$f(k = \chi^2, n_{df}) = \frac{1}{2^{n_{df}/2}\Gamma(n_{df}/2)} k^{\frac{n_{df}}{2}-1} e^{-k/2} \quad (26)$$

Thus, the significance for a given value of  $\chi^2$  called  $\chi_0^2$  is defined as:

$$P(\chi^2 \geq \chi_0^2) = \int_{\chi_0^2}^{+\infty} f(k, n_{df}) dk \quad (27)$$

Note that if  $n_{df} \gg 1$  the  $\chi^2$  distribution  $f(k, n_{df}) \rightarrow$  a Gaussian pdf with mean  $n_{df}$  and variance  $2n_{df}$  [9]. In our case,  $n_j$  are counts so they follow a Poisson distribution that is substantially different from a Gaussian pdf when  $n_j \leq 10$ . Thus, if we want to use the  $\chi^2$  test to check the agreement between data and hypothesis, we have to control if its distribution follows what predicted from the theory.

- All minimization algorithms allow the search for local minimum. The only way to check if we get an absolute one consists of repeating the minimization procedure from different starting points in parameter space.

Starting from the experimental data collected in Config.1, a set of Monte-Carlo pseudo-experiments are developed in order to answer to the previous questions testing the stability and the goodness of the fit procedure:

1. Let's assume that the estimators  $\hat{\tau}^+$  and  $\hat{A}$  are not-biased, so we use their values reported in Eq.25 as expected value for  $\tau^+$  and  $\hat{A}$  in the Monte-Carlo.
2. In each pseudo-experiment, the content of each bin is generated using a Poisson smearing around a expected value given by:<sup>11</sup>

$$\tilde{\nu}_j(\hat{\tau}^+, \hat{A}) = n_{tot} \cdot \int_{t_j^{min}}^{t_j^{max}} f(t, \hat{\tau}^+, \hat{A}) dt \quad (28)$$

---

<sup>11</sup>The random Poisson generator and the uniform one belongs to the class **TRandom3** of ROOT Package <http://root.cern.ch/root/htmldoc/TRandom.html#TRandom>.

3. Each generated spectrum is fitted with the likelihood method previously described. The parameters are initialized using a Monte-Carlo grid around  $\hat{\tau}^+$  and  $\hat{A}$  i.e. before each fit these free parameters are randomly set using a uniform number generator in the intervals  $[\hat{\tau}^+ - 30\% \cdot \hat{\tau}^+, \hat{\tau}^+ + 30\% \cdot \hat{\tau}^+]$ ,  $[\hat{A} - 30\% \cdot \hat{A}, \hat{A} + 30\% \cdot \hat{A}]$ .
4. Finally, the distributions of  $\hat{\tau}^+$  and  $\chi_0^2$  obtained, in this case of  $N = 5000$  pseudo-experiments, are fitted with a Gaussian pdf through the  $\chi^2$  method. These are shown in Fig.25.

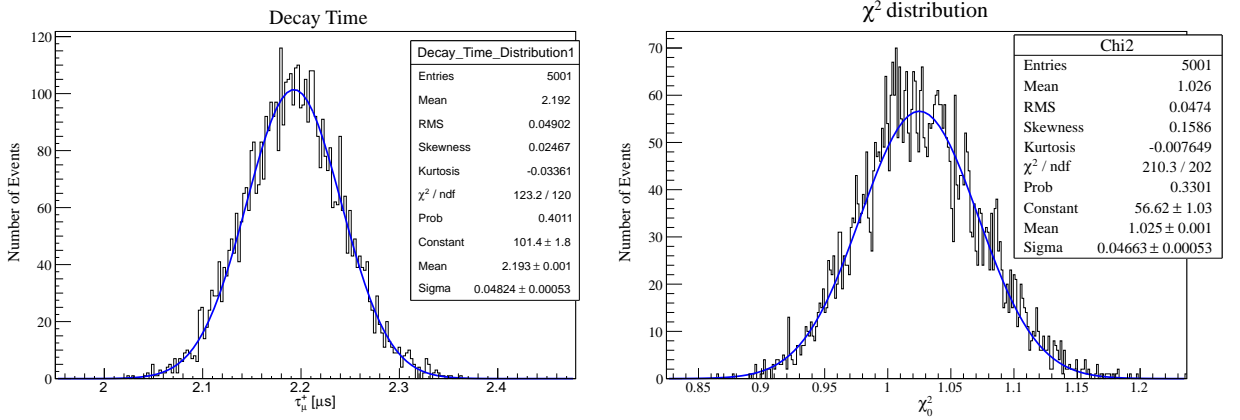


Figure 25: *Left:*  $\hat{\tau}^+$  distribution obtained from the MC simulations. *Right:*  $\chi_0^2$  distribution obtained from the MC simulations.

Analysing the distributions obtained from these simulations, best estimations of  $\hat{\tau}^+$ ,  $\hat{\sigma}_{\tau^+}$  and  $\chi_0^2$  are given by:

$$\boxed{\hat{\tau}^+(C) = 2.193 \mu s \quad \hat{\sigma}_{\tau^+}(C) = 0.048 \mu s} \quad \leftrightarrow \quad \frac{\chi^2}{n_{df}} = 1.026 \quad P(\tilde{\chi}^2 \geq \chi^2) = 40.11\% \quad (29)$$

$$\boxed{\chi_0^2(C) = 1.025 \quad \sigma_{\chi_0^2} = 0.047} \quad \leftrightarrow \quad \frac{\chi^2}{n_{df}} = 1.04 \quad P(\tilde{\chi}^2 \geq \chi^2) = 33.01\% \quad (30)$$

Thus, we have proven how these results are compatible with the properties expected for ML estimators, the  $\chi_0^2$  distribution with  $n_{df} \gg 1$  approximates a Gaussian pdf and that the minimization procedure, for the binned likelihood built on the data, is completely stable after choosing the analysis range  $[0.65, 8.7] \mu s$ . In Fig.26 is shown the distribution of the pull variable defined as:

$$Pull = \frac{\hat{\tau}^+[MC] - \hat{\tau}^+[fit]}{\hat{\sigma}_{\tau^+}[MC]} \quad (31)$$

where  $\hat{\tau}^+[MC]$  is the decay time value derived from the fit in each pseudo-experiment, while  $\hat{\tau}^+[fit]$  is that obtained from the data, reported in Eq.25. If the estimator  $\hat{\tau}^+$  is "regular" and not biased, then the pull variable is normal distributed with  $E[Pull] = 0$  and  $V[Pull] = 1$ . From the pull distribution Gaussian fit, the mean value and the standard deviation are compatible with the expected values at 90% C.L. The bias of mean value can be used as additional systematic uncertainty (2.6%) on the statistic fit procedure.

In addition, we have done a second independent set of pseudo-experiments in which, keeping unchanged the data distribution, we vary the fit range previously fixed in the interval  $[0.65, 8.7] \mu s$ . In each simulation, the range extremes are randomly generated according to a uniform distribution in the gate  $[t_{min} - 250 \text{ ns}, t_{min} + 250 \text{ ns}]$ ,  $[t_{max} - 200 \text{ ns}, t_{max} + 200 \text{ ns}]$  together with a

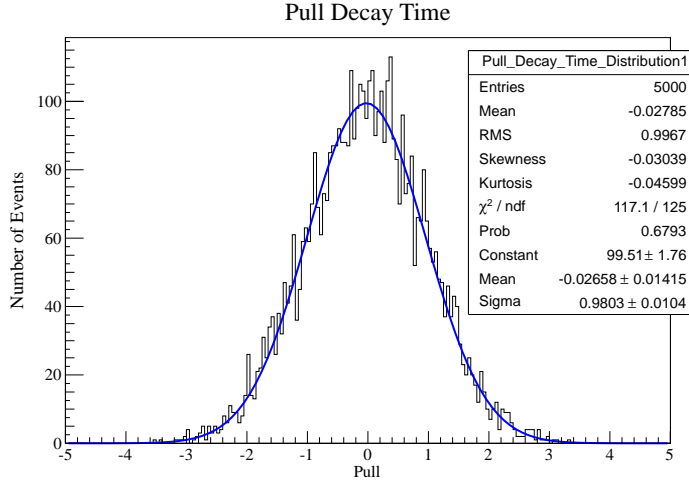


Figure 26: *Pull variable distribution obtained from the MC simulations.*

uniform Monte-Carlo grid on the initial parameters value, as done in the previous simulations. The results are shown in Fig.27, we can see that  $\hat{\tau}^+$  and  $\chi_0^2$  distribution are focused around their previous values, as reported in Eq.25. Thus, the minimization process can be considered stable varying both initial parameters and fit time range because the fluctuations of  $\hat{\tau}^+$  and  $\chi_0^2$  are compatible with the previous values stated in Eq.29 and 30. The RMS of  $\tau^+$  distribution can be considered as an additional systematic uncertainty of the fit procedure. Therefore, considering

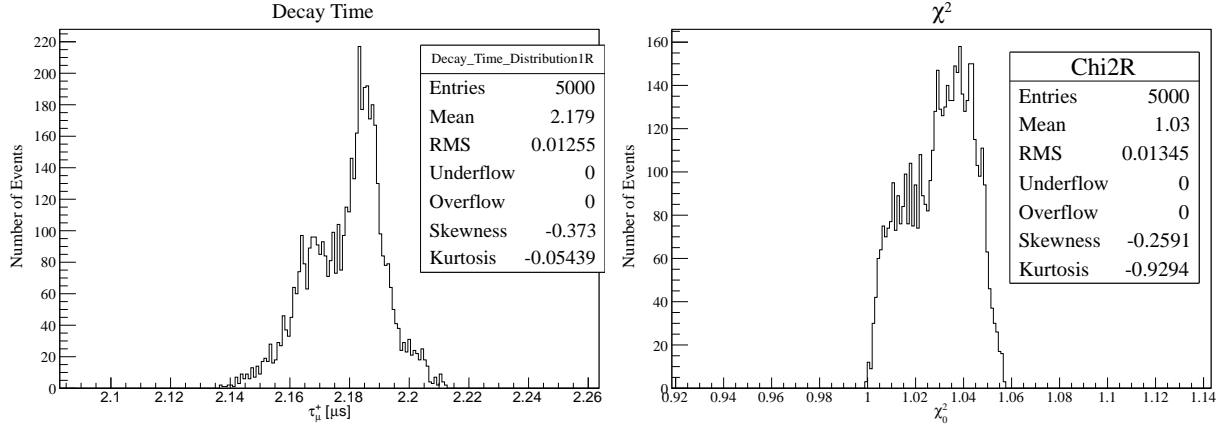


Figure 27: *Left:  $\hat{\tau}^+$  distribution obtained varying the time range. Right:  $\chi_0^2$  distribution obtained from the experimental data varying the time range.*

all the statistical and systematic uncertainties, the final  $\mu$  free lifetime estimation, measured in Config.1, is:

$$\hat{\tau}^+ = 2.193 \pm 0.048(\text{stat.}) \pm 0.058(\text{sys.}) \mu\text{s} \quad (32)$$

that can be considered consistent with the expected one, reported in Eq.2, at 68% C.L.

The same procedure is applied to the collected data in the Config.2, composed of  $n_{tot} = 10668$  decay events. The likelihood fit is performed in the time interval  $[0.9, 8.8] \mu\text{s}$ , using the pdf shown in Eq.21, where B is fixed to the value expected from Eq.18. The time distribution of decay events and the parameters extracted from the fit are reported in Fig.28. The estimates

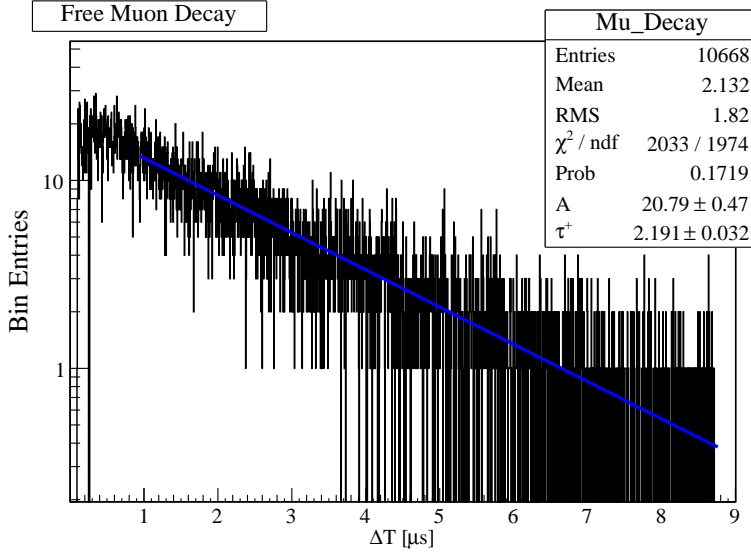


Figure 28: *Fit of free muon decay events in experimental Config. 2.*

obtained for  $A^+$ ,  $\tau^+$  and their errors are:

$$\hat{A}^+ = 20.79 \quad \hat{\sigma}_{A^+} = 0.47 \quad \hat{\tau}^+ = 2.191 \mu s \quad \hat{\sigma}_{\tau^+} = 0.032 \mu s \quad (33)$$

In addition, the errors and the correlation matrix are:

$$V = \begin{pmatrix} \hat{\sigma}_{A^+}^2 = 0.2195 & \hat{\sigma}_{A\tau} = -0.0129 \\ \hat{\sigma}_{\tau A} = -0.0129 & \hat{\sigma}_{\tau^+}^2 = 0.00104 \end{pmatrix} \quad \rho = \begin{pmatrix} \hat{\rho}_{A^+} = 1 & \hat{\rho}_{A\tau} = -0.85 \\ \hat{\rho}_{\tau A} = -0.85 & \hat{\rho}_{\tau^+} = 1 \end{pmatrix}$$

So, for the same reason previously exposed, it is reasonable that the parameters  $A^+$  and  $\tau^+$  are anti-correlated. The agreement between the fitted distribution and the theoretical hypothesis on the pdf is controlled thanks to the  $\chi^2$  test:

$$\chi_0^2 = \frac{\chi^2}{n_{df}} \approx 1.03 \quad P(\tilde{\chi}^2 \geq \chi_0^2) = 17.19 \% \in 95\% \text{ C.L.}$$

As done before, we realize a set of  $N = 5000$  pseudo-experiments in order to give a better estimation for  $\hat{\tau}^+$ ,  $\hat{\sigma}_{\tau^+}$  and  $\chi_0^2$ . The generated distributions are reported in Fig. 29 where they are fitted with a Gaussian pdf using the  $\chi^2$  method; while in Fig. 30 there is the pull decay time distribution obtained thanks to the definition stated in Eq. 31. Analysing them, best estimations of  $\hat{\tau}^+$ ,  $\hat{\sigma}_{\tau^+}$  and  $\chi_0^2$  can be given:

$$\hat{\tau}^+(Pb) = 2.194 \mu s \quad \hat{\sigma}_{\tau^+}(Pb) = 0.026 \mu s \quad \leftrightarrow \quad \frac{\chi^2}{n_{df}} = 0.98 \quad P(\tilde{\chi}^2 \geq \chi^2) = 51.68\% \quad (34)$$

$$\chi_0^2 = 1.116 \quad \sigma_{\chi_0^2} = 0.049 \quad \leftrightarrow \quad \frac{\chi^2}{n_{df}} = 1.04 \quad P(\tilde{\chi}^2 \geq \chi^2) = 32.84\% \quad (35)$$

Thus, these results are in agreement with the expected behavior for ML estimators and the fit can be considered stable in the fixed time interval chosen  $[0.9, 8.8] \mu s$ . The bias of the pull mean value can be used as additional systematic uncertainty (6.5%) on the statistic fit procedure.

In addition, we have studied again the trend of the minimization performance as function of

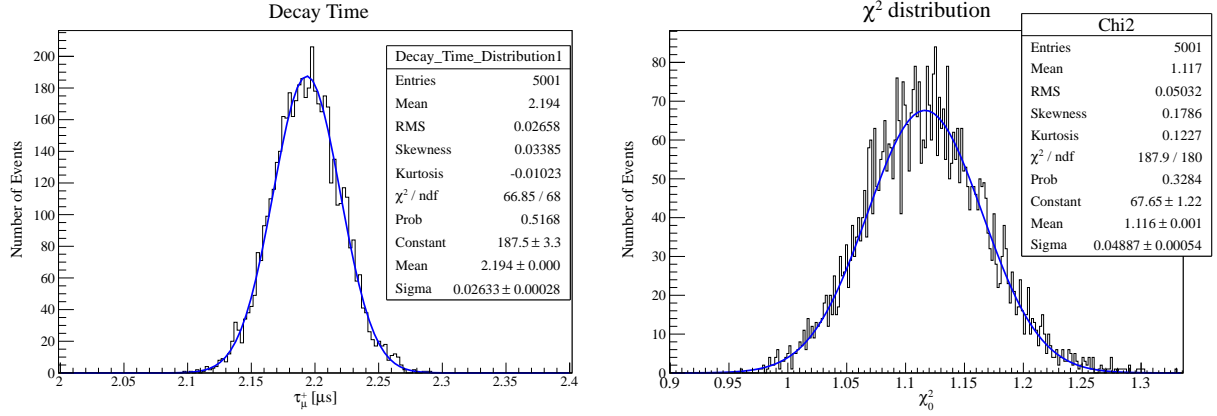


Figure 29: *Left:*  $\hat{\tau}^+$  distribution obtained from the M.C. *Right:*  $\chi^2$  distribution obtained from the M.C.

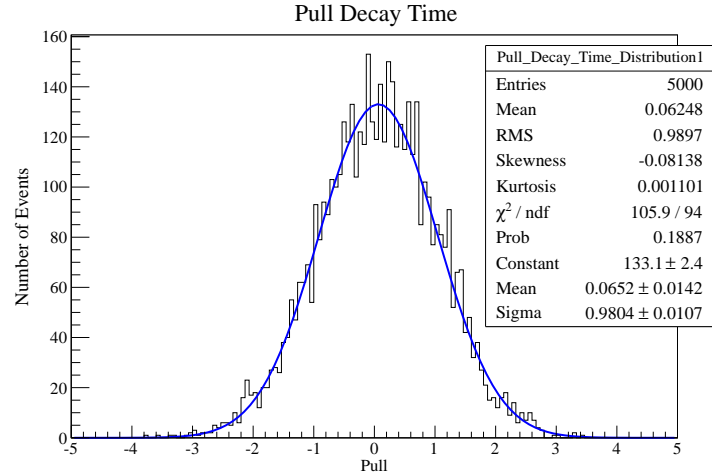


Figure 30: Pull decay time distribution obtained from the M.C simulations.

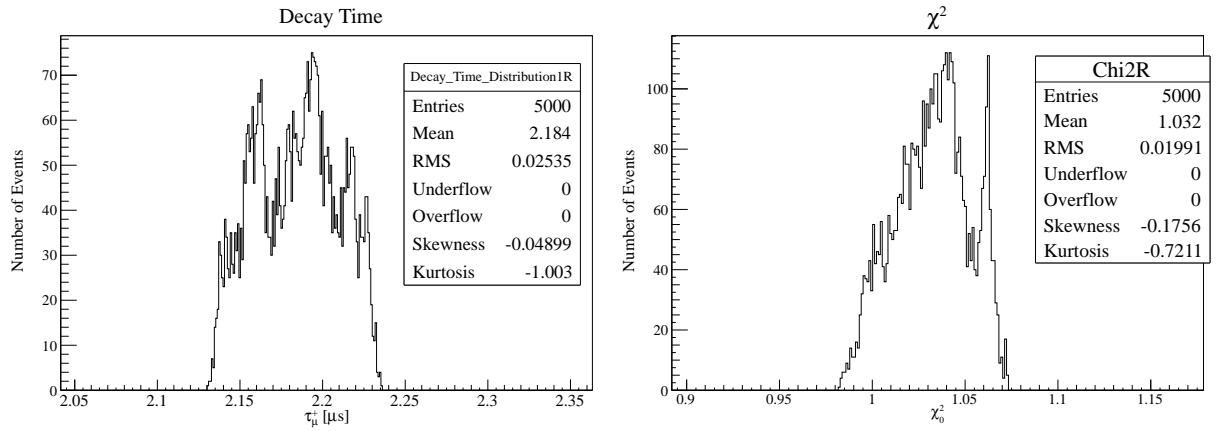


Figure 31: *Left:*  $\hat{\tau}^+$  distribution obtained varying the time range. *Right:*  $\chi^2$  distribution obtained varying the time range.

the time range. So, other 10000 simulations are performed changing any time the fit extremes generating them uniformly in the intervals  $[t_{min} - 500\text{ ns}, t_{min} + 500\text{ ns}]$  and  $[t_{max} - 200\text{ ns}, t_{max} + 200\text{ ns}]$ . The results consist of the  $\hat{\tau}^+$  and the  $\chi_0^2$  distributions shown in Fig.31. Therefore, the minimization process can be considered stable varying both initial parameters and fit time range because the fluctuations of  $\hat{\tau}^+$  and  $\chi_0^2$  are compatible with the measured value reported in Eq.34 and 35. The RMS of  $\tau^+$  distribution can be considered as an additional systematic uncertainty of the fit procedure. Therefore, considering all the statistical and systematic uncertainties, the final  $\mu$  free lifetime estimation, measured in Config.2, is:

$$\hat{\tau}^+ = 2.194 \pm 0.026(\text{stat.}) \pm 0.145(\text{sys.}) \mu\text{s} \quad (36)$$

that can be considered consistent with the expected one, reported in Eq.2, at 68% *C.L.*

## 4.5 Muon lifetime in Aluminium

The muon lifetime in aluminium ( $Al, Z = 13$ ) is measured using the Config.1: the gap between SC2 and SC3 is filled with a slab of aluminum, so the p.d.f of the decay events has the following form:

$$f(B, A^+, A^-, \tau^+, \tau^-) = B + A^+ e^{-t/\tau^+} + A^- e^{-t/\tau^-} \quad (37)$$

The data sample is composed of  $n_{tot} = 18488$  decay events and the Likelihood fit is performed in the time interval between  $[0.29, 8.8]\mu\text{s}$  according to the general distribution reported in Eq.37; where B and  $\tau^+$  are respectively fixed to the values stated by Eq.18 and Eq.2. In Fig.32, the distribution of these decay events and the resulting parameters extracted from the fit are reported.

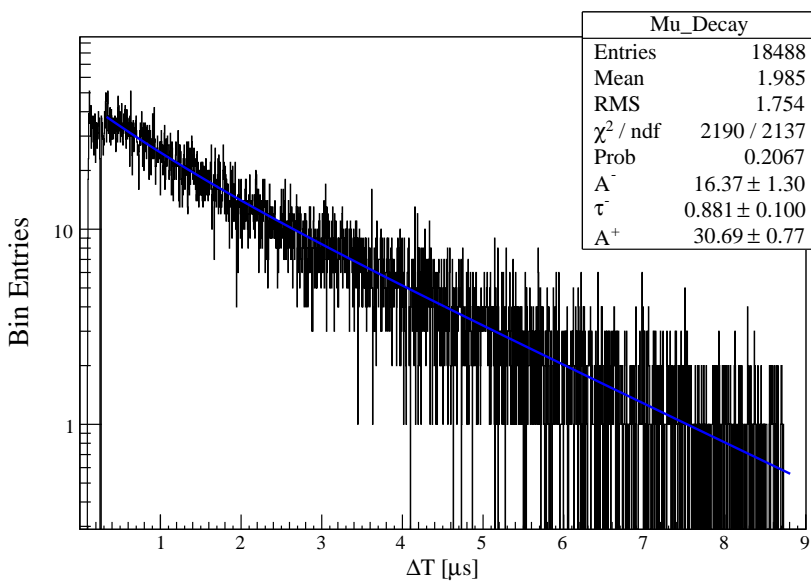


Figure 32: Fit of muon decay events in  $Al$ .

The best estimates obtained for  $A^+$ ,  $A^-$  and  $\tau^-$ , in association with their errors, are:

$$\hat{A}^+ = 30.69 \quad \hat{\sigma}_{A^+} = 0.77 \quad \hat{A}^- = 16.37 \quad \hat{\sigma}_{A^-} = 1.30 \quad \hat{\tau}^- = 881\text{ ns} \quad \hat{\sigma}_{\tau^-} = 100\text{ ns} \quad (38)$$

In addition, the errors and the correlation matrix are:

$$V = \begin{pmatrix} \hat{\sigma}_{A^-}^2 = 1.709 & \hat{\sigma}_{A-\tau} = -0.062 & \hat{\sigma}_{A-A^+} = -0.021 \\ \hat{\sigma}_{\tau A^-} = -0.062 & \hat{\sigma}_{\tau^-}^2 = 0.01 & \hat{\sigma}_{\tau A^+} = -0.0625 \\ \hat{\sigma}_{A^+ A^-} = -0.021 & \hat{\sigma}_{A^+ \tau} = -0.625 & \hat{\sigma}_{A^+}^2 = 0.591 \end{pmatrix}$$

$$\rho = \begin{pmatrix} \hat{\rho}_{A^-} = 1 & \hat{\rho}_{A-\tau} = -0.475 & \hat{\rho}_{A-A^+} = -0.021 \\ \hat{\rho}_{\tau A^-} = -0.475 & \hat{\rho}_{\tau^-} = 1 & \hat{\rho}_{\tau A^+} = -0.811 \\ \hat{\rho}_{A^+ A^-} = -0.021 & \hat{\rho}_{A^+ \tau} = -0.811 & \hat{\rho}_{A^+} = 1 \end{pmatrix}$$

The agreement between the fitted distribution and the theoretical hypothesis on the pdf is checked through the  $\chi^2$  test:

$$\boxed{\chi_0^2 = \frac{\chi^2}{n_{df}} \approx 1.025} \quad P(\tilde{\chi}^2 \geq \chi_0^2) = 20.67\% \in 95\% C.L.$$

After that, a set of  $N = 5000$  pseudo-experiments are realized in order to give a better estimation for  $\hat{\tau}^-$ ,  $\hat{\sigma}_{\tau^-}$  and  $\chi_0^2$  following the procedure exposed in Sec.4.4.1. The resulting distributions of  $\tau^-$  and  $\chi_0^2$  are reported in Fig.33 where they are fitted with a Gaussian pdf using the  $\chi^2$  method. In Fig.34, instead, is shown the distribution of the pull variable defined according to Eq.31. Analysing them, best estimations of  $\hat{\tau}^-$ ,  $\hat{\sigma}_{\tau^-}$  and  $\chi_0^2$  can be given:

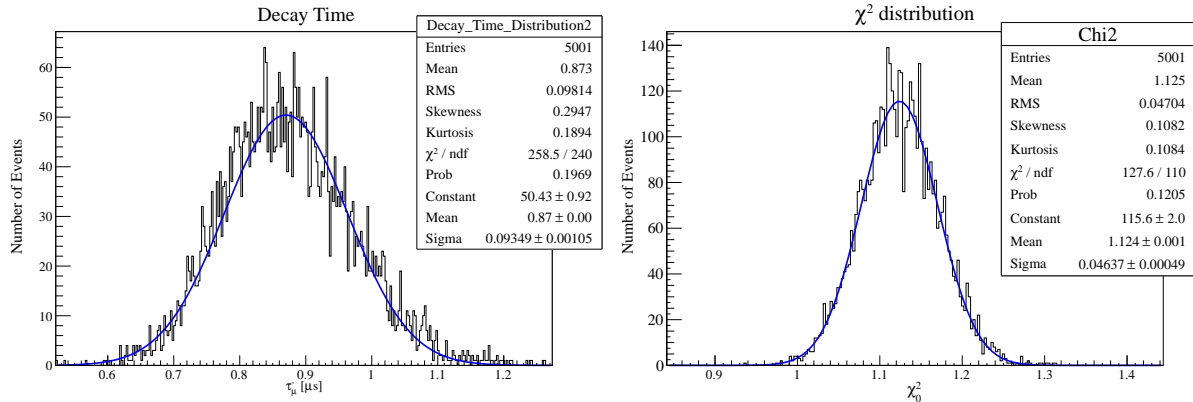


Figure 33: *Left:*  $\hat{\tau}^-$  distribution obtained from the M.C. *Right:*  $\chi_0^2$  distribution obtained from the M.C.

$$\boxed{\hat{\tau}^-(Al) = 870 \text{ ns} \quad \hat{\sigma}_{\tau_\mu^-}(Al) = 93 \text{ ns}} \quad \leftrightarrow \quad \frac{\chi^2}{n_{df}} = 1.08 \quad P(\tilde{\chi}^2 \geq \chi^2) = 19.69\% \quad (39)$$

$$\boxed{\chi_0^2 = 1.124 \quad \sigma_{\chi_0^2} = 0.046} \quad \leftrightarrow \quad \frac{\chi^2}{n_{df}} = 1.16 \quad P(\tilde{\chi}^2 \geq \chi^2) = 12.05\% \quad (40)$$

Thus, these results are in agreement with the expected behaviour for ML estimators and the fit can be considered stable in the fixed time interval chosen  $[0.29, 8.8] \mu\text{s}$ . In Fig.34, the pull variable distribution of  $\tau^-$  is fitted with a Gaussian shape: as already done the mean value can be used as systematic uncertainty (4%) related to the statistical analysis procedure.

The study of the fit behavior varying time ranges is not performed because the inferior fit extreme represent a limit. In fact, if we try to move it to less values, the fit procedure becomes

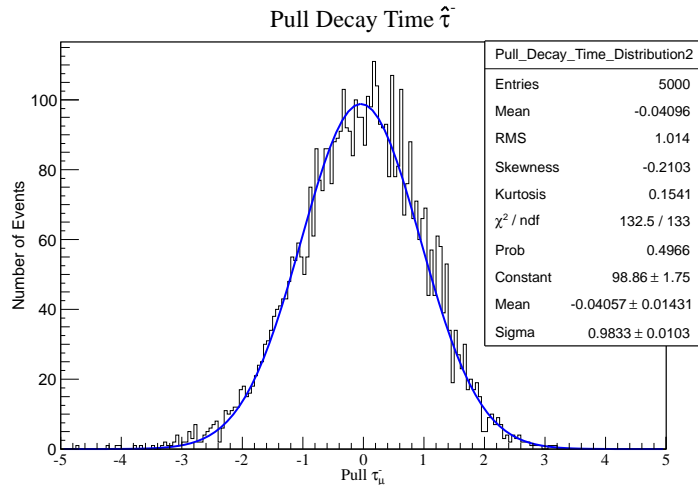


Figure 34: *Pull decay time distribution obtained from the M.C simulations.*

unreliable and not stable. Therefore, considering all the statistical and systematic uncertainties, the final  $\mu^-$  lifetime estimation is:

$$\hat{\tau}^- = 870 \pm 93(\text{stat.}) \pm 35(\text{sys.}) \text{ ns} \quad (41)$$

that can be considered consistent with the expected one, reported in Tab.1, at 68% *C.L.*

## 4.6 Muon lifetime in NaCl

The measure of  $\mu^-$  lifetime in NaCl [(Na,Z=22);(Cl,Z=35)] is different from the previous ones because it is a ionic crystal, so the negative muon can bound either with  $Na^+$  or  $Cl^-$  ions present in the lattice. The time distribution of decay events has still the general form shown in Eq.37, but the value of  $\tau^-$  is not, a priori, well defined and predicted. We can try to predict it assuming that each negative muon has the same probability to bound with a  $Na^+$  or with a  $Cl^-$  ion. So, considering  $\Gamma(Z)$  for Na and Cl atoms reported in Tab.1 and the previous hypothesis, the estimated value for NaCl is given by:

$$\Gamma(NaCl) \approx \frac{\Gamma(Na) + \Gamma(Cl)}{2} \rightarrow \tau^-(NaCl) = 743 \text{ ns} \quad (42)$$

The sample of data collected (the experimental setup coincide with the Config.1) consists of  $n_{tot} = 10897$  decay events, as shown in Fig.35. The likelihood fit is performed in the time interval  $[0.29, 8.75]\mu\text{s}$ , using the same pdf reported in Eq.37.  $B$  and  $\tau^+$  are fixed as the values:  $B$  according to Eq.18 while  $\tau^+$  as stated in Eq.2. Thus, there are three free parameters in the fit:  $A^+$ ,  $A^-$  and  $\tau^-$ . These are the values and the errors obtained :

$$\hat{A}^+ = 19.26 \quad \hat{\sigma}_{\hat{A}^+} = 0.46 \quad \hat{A}^- = 8.367 \quad \hat{\sigma}_{\hat{A}^-} = 1.368 \quad \hat{\tau}_\mu^- = 702 \text{ ns} \quad \hat{\sigma}_{\hat{\tau}_\mu^-} = 139 \text{ ns}$$

In addition, the errors and the correlation matrix are:

$$V = \begin{pmatrix} \hat{\sigma}_{A^-}^2 = 1.454 & \hat{\sigma}_{A^- \tau} = -0.109 & \hat{\sigma}_{A^- A^+} = -0.053 \\ \hat{\sigma}_{\tau A^-} = -0.109 & \hat{\sigma}_{\tau}^2 = 0.021 & \hat{\sigma}_{\tau A^+} = -0.051 \\ \hat{\sigma}_{A^+ A^-} = -0.053 & \hat{\sigma}_{A^+ \tau} = -0.051 & \hat{\sigma}_{A^+}^2 = 0.224 \end{pmatrix}$$

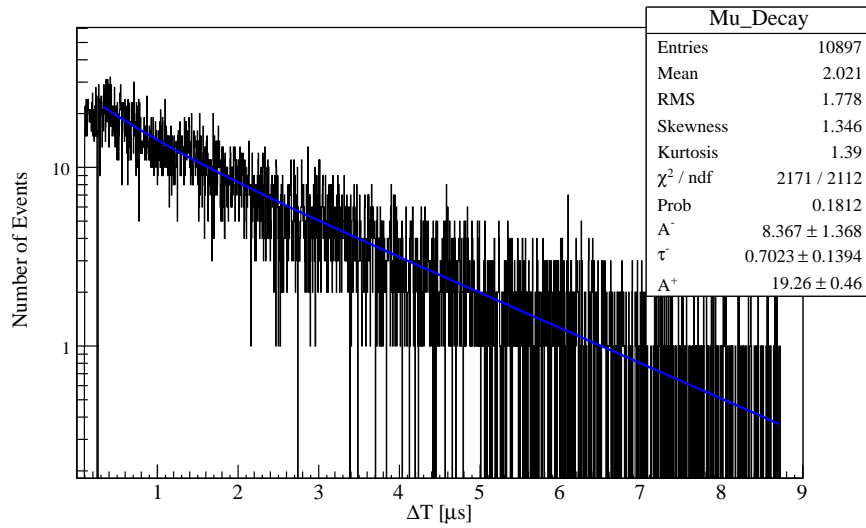


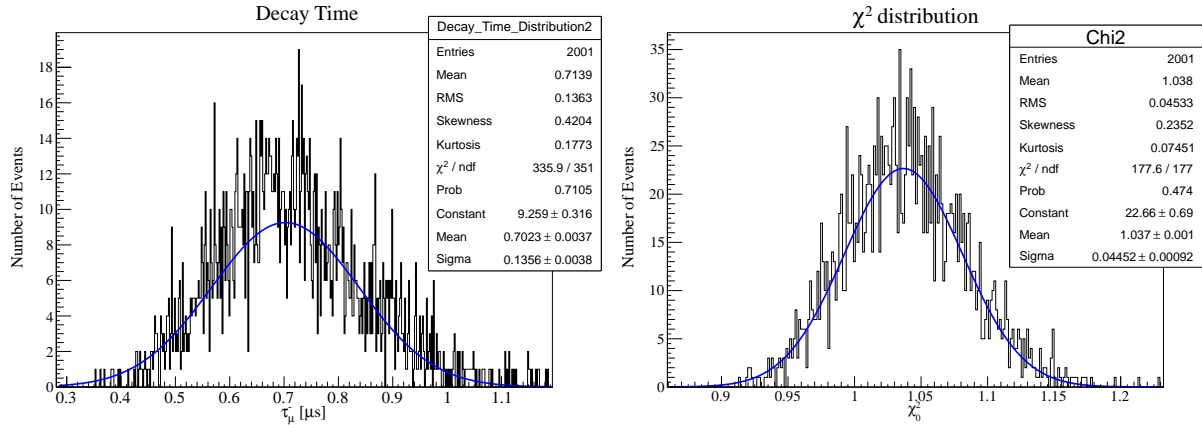
Figure 35: Fit of bound muon decay events in NaCl.

$$\rho = \begin{pmatrix} \hat{\rho}_{A^-} = 1 & \hat{\rho}_{A-\tau} = -0.634 & \hat{\rho}_{A-A^+} = -0.093 \\ \hat{\rho}_{\tau A^-} = -0.634 & \hat{\rho}_{\tau^-} = 1 & \hat{\rho}_{\tau A^+} = -0.747 \\ \hat{\rho}_{A^+ A^-} = -0.093 & \hat{\rho}_{A^+ \tau} = -0.747 & \hat{\rho}_{A^+} = 1 \end{pmatrix}$$

The  $\chi^2$  value and its probability, obtained from the fit, are:

$$\boxed{\chi_0^2 = \frac{\chi^2}{n_{df}} = 1.028} \quad P(\tilde{\chi}^2 \geq \chi_0^2) = 18.12\% \in 95\% C.L.$$

As largely exposed in the Sec.4.4.1, also here a set of  $N = 2000$  independent pseudo-experiment is developed in order to check the stability and the goodness of the fit estimators. The resulting distributions of  $\tau^-$  and  $\chi_0^2$  are reported in Fig.36 where they are fitted with a Gaussian pdf using the least squared method. In Fig.37, instead, is shown the distribution of the pull variable

Figure 36: Left:  $\hat{\tau}^-$  distribution obtained from the M.C. Right:  $\chi_0^2$  distribution obtained from the M.C.

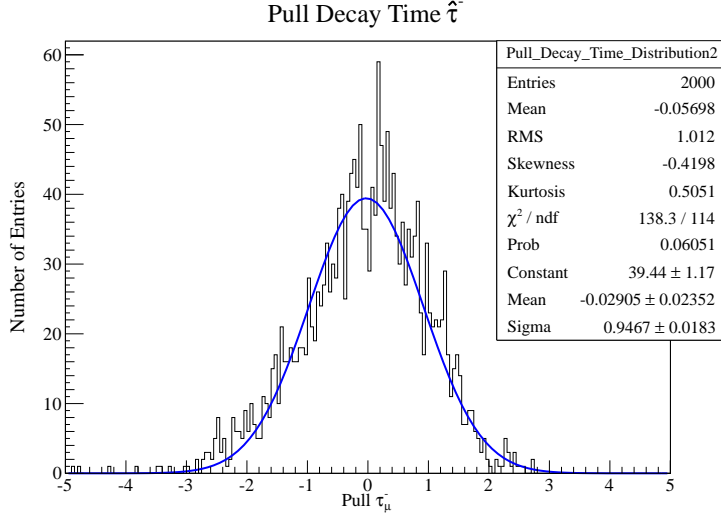


Figure 37: Pull decay time distribution obtained from the M.C simulations.

defined according to Eq.31. Analysing them, best estimations of  $\hat{\tau}^-$ ,  $\hat{\sigma}_{\tau^-}$  and  $\chi_0^2$  are given by:

$$\boxed{\hat{\tau}^-(NaCl) = 702 \text{ ns} \quad \hat{\sigma}_{\tau^-}(Al) = 136 \text{ ns}} \quad \leftrightarrow \quad \frac{\chi^2}{n_{df}} = 0.957 \quad P(\tilde{\chi}^2 \geq \chi^2) = 71.05\% \quad (43)$$

$$\boxed{\chi_0^2 = 1.037 \quad \sigma_{\chi_0^2} = 0.044} \quad \leftrightarrow \quad \frac{\chi^2}{n_{df}} = 1.003 \quad P(\tilde{\chi}^2 \geq \chi^2) = 47.40\% \quad (44)$$

Thus, these results are in agreement with the expected behaviour for ML estimators and the fit can be considered stable in the fixed time interval chosen  $[0.29, 8.75] \mu\text{s}$ . The pull variable distribution of  $\tau^-$  is fitted with a Gaussian shape: as already done the mean value can be used as systematic uncertainty (2.9%) related to the statistical analysis procedure.

In addition, we have also studied the trend of the minimization procedure as function of the time range. Therefore,  $N = 1000$  simulations are performed changing any time the fit extremes generating them uniformly in the intervals  $[t_{min}, t_{min} + 200 \text{ ns}]$  and  $[t_{max} - 200 \text{ ns}, t_{max} + 200 \text{ ns}]$ , asymmetric respect to the central point  $t_{min}$ . This is because, below  $t_{min} = 0.29 \mu\text{s}$  the distribution of data shifts from the expected one and the fit becomes instable. The results consist of the  $\hat{\tau}^-$  and the  $\chi_0^2$  distributions shown in Fig.38. Therefore, the minimization process can be considered stable varying both initial parameters and fit time range because the fluctuations of  $\hat{\tau}^+$  and  $\chi_0^2$  are compatible with the measured value reported in Eq.43 and 44. The RMS of the  $\tau^-$  distribution can be considered as an additional systematic uncertainty of the fit procedure. Therefore, considering all the statistical and systematic uncertainties, the final  $\mu^-$  lifetime estimation, measured in Config.1, is:

$$\boxed{\hat{\tau}^-(NaCl) = 702 \pm 136(\text{stat.}) \pm 52(\text{sys.}) \text{ ns}} \quad (45)$$

that can be considered consistent with the expected one, reported in Eq.42, at 68% C.L.

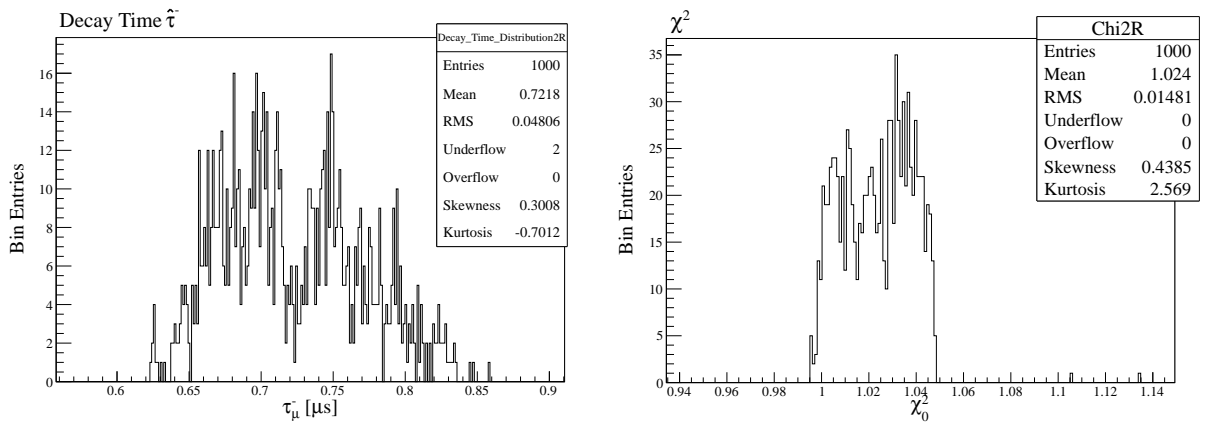
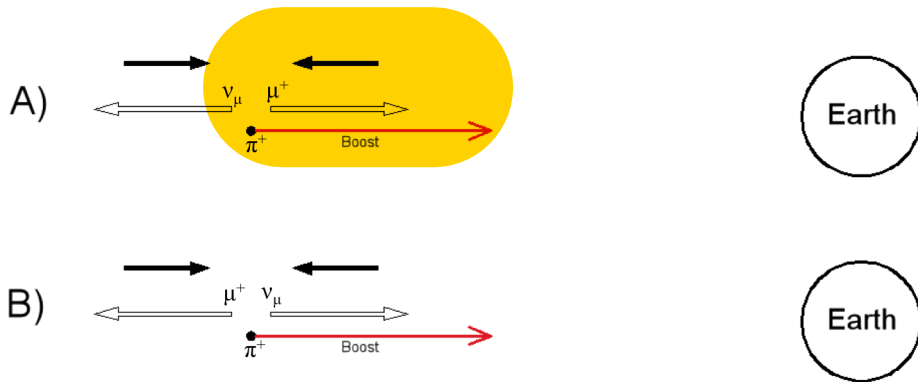
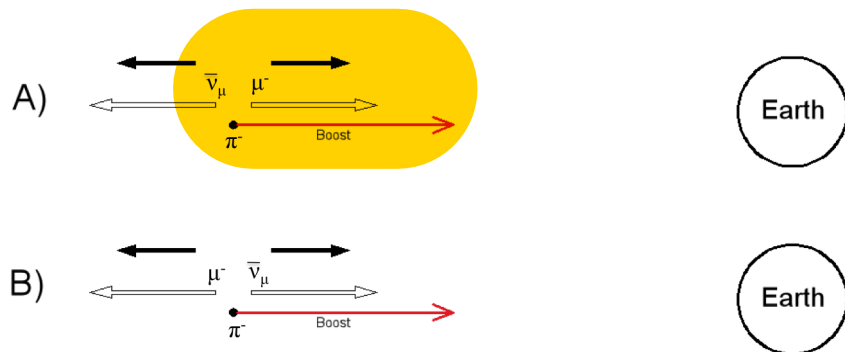


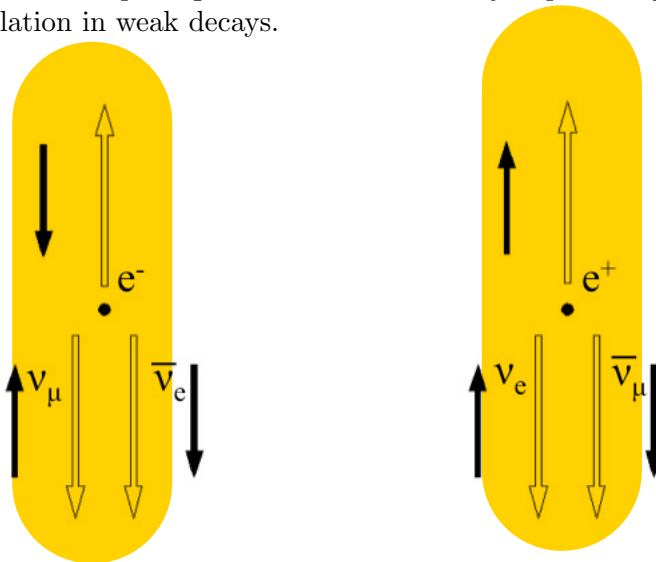
Figure 38: *Left:*  $\hat{\tau}^-$  distribution obtained varying the time range. *Right:*  $\chi^2_0$  distribution obtained from the experimental data varying the time range.

## 5 Polarized Muon Decay

As we have already said, the muons we study in this experiment are originated by cosmic rays. In particular they come from reactions:  $\pi^\pm \rightarrow \mu^\pm + \nu_\mu (\bar{\nu}_\mu)$ . These ones involve high energy pions, which are generated in the high atmosphere and are mainly directed toward the Earth surface. Pions direction is determined by the initial direction of the incident cosmic protons. When the pion decays, in its rest frame, the muon can be emitted in any direction. For sake of simplicity, we analyse the two extreme cases: when the muon is emitted in the same direction of the pion's boost and when the muon is emitted in the opposite direction, as shown in Fig.39. In the case A)  $\mu^+$  is directed forward (toward the Earth) and  $\nu_\mu$  is directed in the opposite direction, due to the conservation of spatial momentum in the pion's rest frame. In this case the pion boost is directed in the same direction of the  $\mu^+$ . Since the neutrino has a fixed helicity, *left-handed*, the total angular momentum conservation forces also the  $\mu^+$  to be *left-handed* ( $\mu_L^+$ ); indeed,  $\mu^+$  has the spin oriented in the opposite direction to the neutrino spin. *Mutatis mutandis*, in case B)  $\mu^+$  has the spin oriented in the boost direction. Note that all anti-muons of configuration B) in the laboratory frame change their helicity becoming *right-handed* ( $\mu_R^+$ ). If we consider the laboratory frame, it's remarkable that in order to reach the ground muons emitted backward in the pion rest frame need more energy than ones emitted in the same direction of the boost. Since the muon energy spectrum decreases with energy, the majority muons in laboratory are the forward ones. Everything said so far is also valid for  $\mu^-$ , see Fig.40, with the difference that anti-neutrino is *right-handed*, so less energetic  $\mu^-$  are *right-handed* ( $\mu_R^-$ ) and more energetic  $\mu^-$  are *left-handed* ( $\mu_L^-$ ). Therefore, we expect that at the sea level  $\mu^-$  are mainly *right-handed* and  $\mu^+$  are mainly *left-handed*. Experimentally, this fact is correlated with the measured mean cosmic muons degree of polarization:  $\xi^- = 0.35 \pm 0.02$  for  $\mu^-$  and  $\xi^+ = -0.35 \pm 0.02$  for  $\mu^+$ [10]. Muons initial polarization is correlated with the direction of electrons and positrons emitted in the decay. Furthermore, it's possible to detect only  $e^\pm$  with enough energy to pass the thresholds, so for sake of simplicity we concentrate on decay events with most energetic  $e^\pm$  where it is emitted in the opposite direction of both neutrinos. For each type of decay  $\mu^+ \rightarrow e^+ + \nu_e + \bar{\nu}_\mu$ ,  $\mu^- \rightarrow e^- + \bar{\nu}_e + \nu_\mu$  we analyse the two extreme case: the  $e^\pm$  is emitted upward respect to scintillator plane, or the  $e^\pm$  is emitted downward respect to scintillator plane. If we consider that all  $\mu^-$  are right-handed, since the Feynman amplitude for the polarized decay  $\mu^- \rightarrow e^- + \nu_\mu + \bar{\nu}_e$  depends on  $1 - \vec{\eta} \cdot \vec{p}_e$ , the probability is maximum when  $\vec{\eta} \cdot \vec{p}_e = -1$  (electron momentum anti-parallel to muon spin). *Vice versa*, for the process  $\mu^+ \rightarrow e^+ + \nu_e + \bar{\nu}_\mu$ , the matrix element depends

Figure 39:  $\pi^+$  decay scheme.Figure 40:  $\pi^-$  decay scheme.

on  $1 + \vec{\eta} \cdot \vec{p}_e$ , so is more favourite the emission of positron parallel to  $\mu^+$  spin. In Fig.41 are reported the most favourite configurations for each decay mode. In both cases the  $e^\pm$  is emitted preferably upwards: this is a simple argument which shows why a spatial asymmetry distribution is related to parity violation in weak decays.

Figure 41: Left: most favourite configuration for the decay mode  $\mu^- \rightarrow e^- + \bar{\nu}_e + \nu_\mu$ ; Right: most favourite configuration for the decay mode  $\mu^+ \rightarrow e^+ + \nu_e + \bar{\nu}_\mu$ .

## 5.1 Polarized muon decay rate

Consider a muon with momentum  $p_\mu$  and the spin directed along the unit vector  $\vec{\eta}$ . The helicity projectors for Dirac fermion are defined as:

$$\hat{\Pi}^\pm(p) = \frac{1}{2}(1 \pm \hat{\sigma}_p) \quad \hat{\sigma}_p = \frac{\vec{p} \cdot \vec{\sigma}}{|\vec{p}|} \xrightarrow{m \rightarrow 0} \hat{\Pi}^\pm(p) = \frac{1}{2}(1 \pm \gamma^5) \quad (46)$$

In the rest frame of a particle is possible to define, in a covariant way, a spin projection operator along a direction  $\vec{\eta}$  introducing the space-like vector  $\eta^\mu(0, \vec{\eta})$ , which has the following properties:

$$\eta^2 = -1 \quad \eta^\mu \cdot p_\mu = 0$$

So, the required spin projection operators are [11]:

$$\hat{\Pi}^\pm(\eta) = \frac{1}{2}(1 \pm \not{\eta}\gamma^5) \quad (47)$$

The Feynman amplitude at L.O. for polarized  $\mu^-$  decay becomes (see Eq.76):

$$M = -\frac{G_f}{\sqrt{2}} \left[ \bar{u}_{r'}(p_{\nu_\mu}) \gamma^\mu (1 - \gamma^5) \hat{\Pi}^+(\eta) u(p_\mu) \right] \left[ \bar{u}_s(p_e) \gamma_\mu (1 - \gamma_5) v_{s'}(p_{\nu_e}) \right] \quad (48)$$

$$\sum_{r',s,s'} |M|^2 = \frac{G_f^2}{4} Tr \left[ \not{\psi}_{\nu_\mu} \gamma^\mu (1 - \gamma^5) (\not{p}_\mu - m_\mu \not{\eta}\gamma^5) \gamma^\nu (1 - \gamma^5) \right] Tr \left[ \not{\psi}_e \gamma_\mu (1 - \gamma_5) \not{\psi}_{\nu_e} \gamma_\nu (1 - \gamma_5) \right]$$

that brings to:

$$\sum |M|^2 = 64G_f^2 \left[ (p_{\nu_\mu} \cdot p_e)(p_{\nu_e} \cdot p_\mu) - m_\mu (p_{\nu_\mu} \cdot p_e)(p_{\nu_e} \cdot \eta) \right] \quad (49)$$

Note that the left therm in Eq.49 is common with the unpolarized process, while the right ones is obtained by replacing  $p_\mu$  with  $\eta$ . Thus, repeating the same passages done for the unpolarized decay, the electron spectrum takes the following form:

$$E_e \frac{d\Gamma}{d^3 p_e} = \frac{2\pi}{3(2\pi)^5 m_\mu} \left[ Q^2 (p_e \cdot p_\mu) + 2(Q \cdot p_\mu)(Q \cdot p_e) - m_\mu \left( Q^2 (p_e \cdot \eta) \pm 2(Q \cdot \eta)(Q \cdot p_e) \right) \right] \quad (50)$$

where  $\pm$  underline the difference between  $\mu^-$  and  $\mu^+$  decay<sup>12</sup>. Finally, being  $Q = p_\mu - p_e$  and in the limit  $m_e \rightarrow 0$ , we obtain:

$$\frac{d\Gamma}{dx d\Omega} = \frac{1}{2\pi\tau^+} x^2 \left[ (3 - 2x) \pm \vec{\eta} \cdot \hat{p}_e (1 - 2x) \right] \quad (51)$$

If we consider the mean degree muons polarization, we have to scale  $\eta \cdot \hat{p}_e$  with  $\xi = |\xi^+| = |\xi^-| = 0.35$ . Integrating over  $\phi \in [0, 2\pi]$  and  $x \in [0, 1]$ , with  $\xi \cdot \vec{\eta} \cdot \hat{p}_e = \xi |\vec{\eta}| |\hat{p}_e| \cos \theta = \xi \cos \theta$ :

$$\frac{d\Gamma_{\mu^+}}{d\cos \theta} = \frac{1}{2\tau^+} \left[ 1 + \frac{\xi}{3} \cos \theta \right] \quad (52)$$

$$\frac{d\Gamma_{\mu^-}}{d\cos \theta} = \frac{1}{2\tau^+} \left[ 1 - \frac{\xi}{3} \cos \theta \right] \quad (53)$$

Studying this process is clear that parity  $\hat{P}$  isn't good symmetry for electroweak process. Parity is violated because the decay rate isn't symmetric under parity transformation  $\frac{d\Gamma}{d\cos \theta} \propto (1 \pm \frac{\xi}{3} \cos \theta)$ .

<sup>12</sup>This is due to the different energy projectors extracted in  $M(\mu^-) \rightarrow (\not{\psi}_\mu + m_\mu)$  and  $M(\mu^+) \rightarrow (\not{\psi}_\mu - m_\mu)$

## 5.2 Interaction with a Magnetic Field

The simple way to align the muon spin along a chosen direction is to exploit the interaction between the muon magnetic dipole momentum and an external magnetic field  $\vec{B}$ . In Quantum Mechanics the Hamiltonian of a free charged particle, with spin  $\hat{S}$  and orbital angular momentum  $\hat{L}$ , in interaction with a E-M field is given by:

$$\hat{H} = \frac{(\hat{p} - q\hat{A})^2}{2m} + q\phi - \vec{\mu}_S \cdot \vec{B} \xrightarrow{\nabla \cdot \vec{A} = 0, \vec{B} = B_0 \hat{n}} \hat{H} = \hat{H}_0 + \hat{H}_{int} = \frac{\hat{p}^2}{2m} - (\vec{\mu}_L + \vec{\mu}_S) \cdot \vec{B} \quad (54)$$

where  $\vec{\mu}_S$  is given by:

$$\vec{\mu}_S = \frac{e}{2mc} g_s \vec{S}$$

The stationary Schrödinger equation in a uniform magnetic field (to simplify we assume  $\vec{B} = B_0 \hat{k}$ ), can be easily solved applying the “asymmetric choice” [12], thus the solution consists of a linear harmonic oscillator along the transverse plane, respect to the direction of  $\vec{B}$ , with frequency:

$$\omega = \frac{eB_0}{m_\mu c} \quad (55)$$

The result of this coupling is the precession of the muon spin  $\vec{S}$  around the direction of the magnetic field  $\hat{k}$ , with frequency  $\omega$ .

## 5.3 Muon Decay in a Uniform Magnetic Field

If we want to calculate the muon decay rate in a uniform magnetic field, remembering what was said in Sec.5.2, we have to correct the spin projection operator in Eq.47 with the precession effect:

$$\hat{\Pi}^\pm(\eta) = \frac{1}{2}[1 \pm \gamma^5 \cos \omega t] \quad (56)$$

Repeating the same procedure exposed in Sec.5.1, we obtain:

$$\frac{d\Gamma_{\mu^+}}{d \cos \theta} = \frac{1}{2\tau^+} \left[ 1 + \frac{\xi}{3} \cos \theta \cos \omega t \right] \quad (57)$$

$$\frac{d\Gamma_{\mu^-}}{d \cos \theta} = \frac{1}{2\tau^+} \left[ 1 - \frac{\xi}{3} \cos \theta \cos \omega t \right] \quad (58)$$

Because of the different polarization between positive and negative muons, events with electron emitted in the upper hemisphere (up-events) are obtained for  $\mu^+$  integrating in Eq.57  $\cos \theta \in [0, 1]$  and down events integrating in Eq.57  $\cos \theta \in [-1, 0]$ ; on the other hand, for  $\mu^-$  up-events are obtained integrating in Eq.58  $\cos \theta \in [-1, 0]$  and down-events integrating in Eq.58  $\cos \theta \in [0, 1]$ :

$$\begin{aligned} \Gamma(t)_{\mu^+}^{up} &= \frac{1}{2\tau^+} \left[ 1 + \frac{\xi}{6} \cos \omega t \right] & \Gamma(t)_{\mu^+}^{down} &= \frac{1}{2\tau^+} \left[ 1 - \frac{\xi}{6} \cos \omega t \right] \\ \Gamma(t)_{\mu^-}^{up} &= \frac{1}{2\tau^+} \left[ 1 + \frac{\xi}{6} \cos \omega t \right] & \Gamma(t)_{\mu^-}^{down} &= \frac{1}{2\tau^+} \left[ 1 - \frac{\xi}{6} \cos \omega t \right] \end{aligned}$$

Note that there's no difference between  $\Gamma_{\mu^+}$  and  $\Gamma_{\mu^-}$ .

$$\Gamma_{tot} = \Gamma^{up} + \Gamma^{down} = \int_0^{4\pi} \frac{1}{4\pi\tau^+} \left[ 1 \pm \frac{\xi}{3} \cos \theta \cos \omega t \right] d\Omega = \frac{1}{\tau^+} \quad (59)$$

Since  $-dN = N\Gamma_{tot}dt$  and  $\frac{\Gamma^{up/down}(t)}{\Gamma_{tot}}$  is the probability to find a decay electron in the related acceptance zone:

$$U(t) = \frac{dN^{up}}{dt} = \frac{N_0}{2\tau^+} \left[ 1 + \frac{\xi}{6} \cos \omega t \right] e^{-t/\tau^+} \quad (60)$$

$$D(t) = \frac{dN^{down}}{dt} = \frac{N_0}{2\tau^+} \left[ 1 - \frac{\xi}{6} \cos \omega t \right] e^{-t/\tau^+} \quad (61)$$

Thus, we can define an asymmetry variable between up and down decay events:

$$A(t) = \frac{U(t) - D(t)}{U(t) + D(t)} = \frac{\xi}{6} \cos \omega t \quad (62)$$

## 6 Asymmetry measurement

In this section we describe how to perform an asymmetry measurement. As our goal is to measure the parity violation in muon's decay, the Larmor precession frequency of the muon spin in a known magnetic field is apt to this performance. After all the considerations made in Sec. 5, the muon spin orientation is related to the decay product ( $e^\pm$ ) direction. In order to make this, the used setting is shown in Fig.42 where SC2 is placed inside a copper solenoid to generate a uniform magnetic field. The electronic chain is almost the same described in Sec.4,

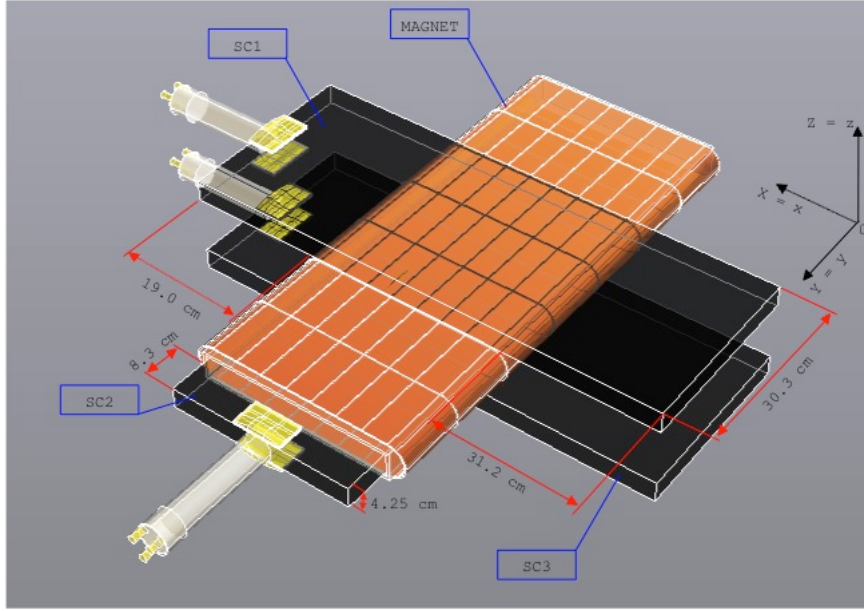


Figure 42: Experimental setting for asymmetry measurement.

but the coincidences are changed: start topology is  $SC1 \times SC2 \times \overline{SC3}$  and stop topology is  $SC1 \times SC2 \times \overline{SC3}$  (Up-events) and  $\overline{SC1} \times SC2 \times SC3$  (Down-events). Since each start is also an up-stop-event, we maintain the same start-stop delay chosen in Sec.4.2. Therefore, the aim of this electronic setting is to detect only muons decayed inside the scintillator SC2 and we are also able to determine if the  $e^\pm$  is emitted in the up region (signal on SC1) or in the down region (signal on SC3). As we want to measure the most oscillation-sensible quantity, the distributions of down and up events are not apt to it. The best choice is to measure the asymmetry defined in Eq.62. Positives muons can't bind, so they only decay free with a lifetime  $\tau^+$ , on the other

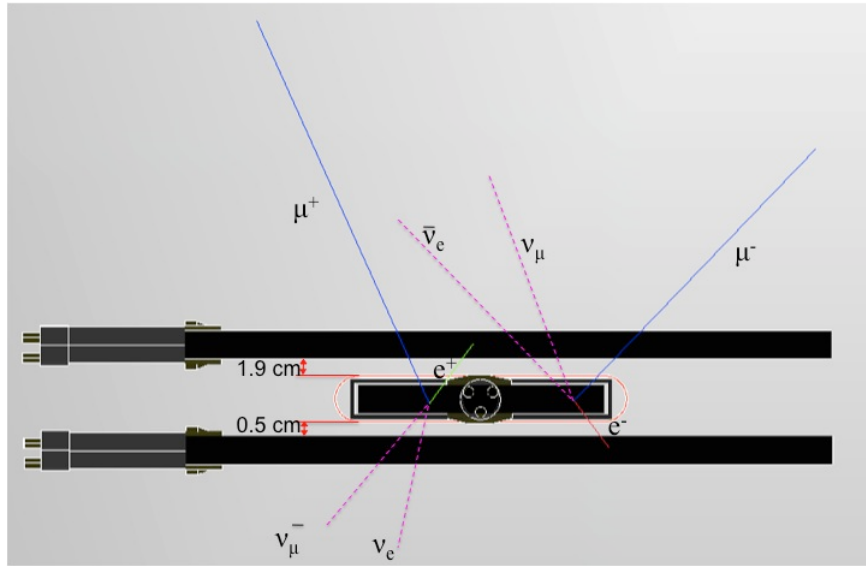


Figure 43: Example of muon decay events in the experimental apparatus.

hand, negative muons can decay free or can decay in a bound state. When  $\mu^-$  decay in a bound state they lose polarization modifying the total asymmetry.

## 6.1 Magnetic field characterization

As shown in Fig.42, SC2 is inserted in a solenoid; this magnet creates a solenoidal magnetic field which is expected to be as uniform as possible. In order to verify the field uniformity, Hall-effect magnetic probes are used. The solenoid is supplied with a current generator, thus first of all, it is necessary to prove the linearity:

$$B(I) = \mu n I$$

where  $\vec{B}$  is:

$$\vec{B} = \begin{pmatrix} 0 \\ B_y(x, y, z) \\ 0 \end{pmatrix} \quad (63)$$

As shown in Fig.44 the linearity between the magnetic field intensity  $B$  and the current  $I$  is well verified. Secondly, we have the probe slide in the magnet so that the field on the  $xy$ -plane can be measured, see Fig.42. Since the probe is lifted up of about 2 cm (half of the scintillator thickness) from the ground, the measure on the  $z$ -axis is not performed. However, some trials are done shifting the probe along  $z$ -axis for other 2 cm, obtaining  $B$  values compatible with the previous ones within the instrument sensibility (0.5 G), so  $B_y(x, y, z) \rightarrow B_y(x, y)$ . So, the uncertainty on transverse direction is fixed to  $\sigma_{B_x} = 0.5$  G. In Fig.45 the shape of  $B$  field on the  $xy$ -plane is shown. As you can see, near the fringes the field decreases, whilst from about 20 cm to 60 cm on the  $y$ -axis it is almost constant. For this reason, to evaluate an average field, for six  $x$ -fixed values  $[x_i]$  we mediated  $B_y(x_i, y)$  along  $y$  from 20 cm to 60 cm. Finally, we fitted this six values with a constant function, as shown in Fig.46. The measured mean value is:  $B = 33.58 \pm 0.11$  G. The additional uncertainty on  $z$ -axis gives:

$$B = 33.58 \pm 0.51 \text{ G} \quad (64)$$

From Larmor frequency definition Eq.55:

$\omega = 2.841 \pm 0.043 \text{ MHz}$

(65)

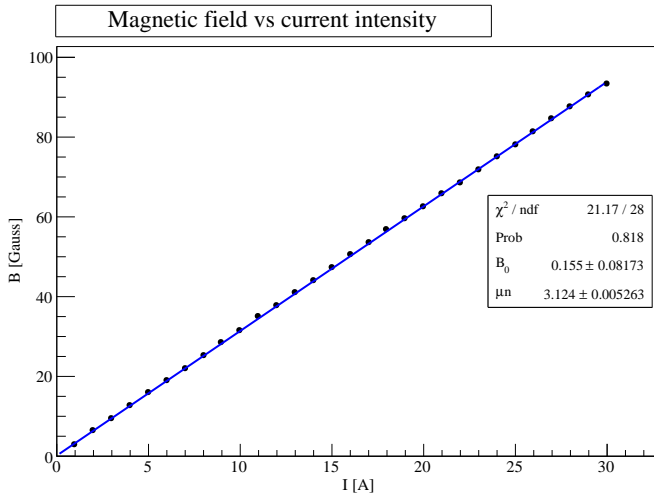


Figure 44: *Magnetic field measured dependence as function of current intensity.*

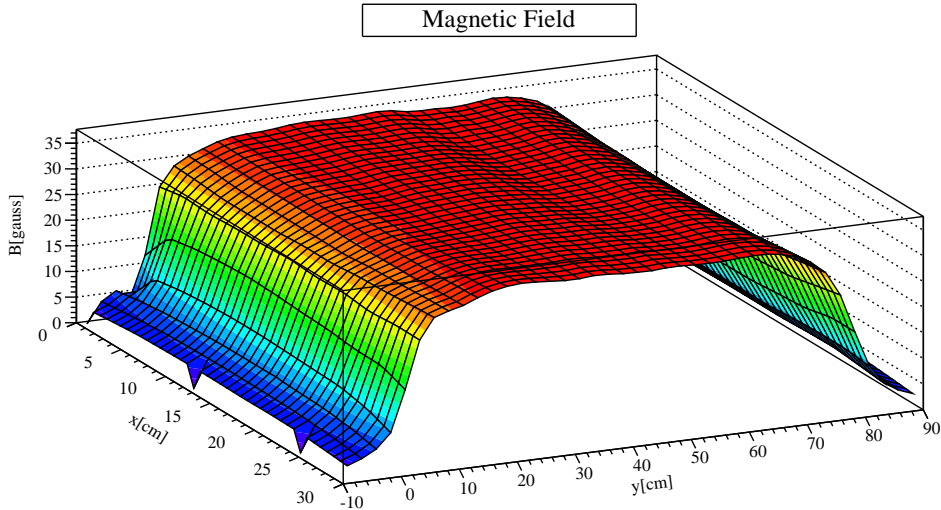


Figure 45: *Solenoid inner magnetic field on xy plane.*

## 6.2 Data analysis

In order to be coherent with the experimental data, the asymmetry relation in Eq.62 has to be corrected by different systematics sources:

- Since the scintillators have finite dimensions, the acceptance it's not unitary, thus in the integration of Eq.51 the solid angle is not  $4\pi$ . The geometry of the system is showing in Fig.42, where  $z=h$  is fixed to the distance between  $SC2$  and one of the other two scintillator; so it's possible to calculate the effective solid angle making a change of variables:

$$\sin \theta d\theta d\phi = \frac{h}{(x^2 + y^2 + h^2)^{\frac{3}{2}}} dx dy$$

Taking into account that the muon can decay inside all the  $SC2$  volume, calling  $(X, Y, Z)$

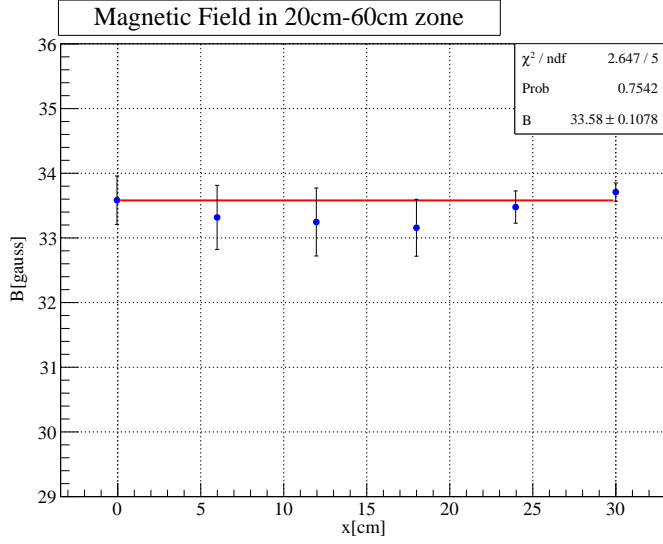


Figure 46: Average magnetic field in the solenoid.

the muon position in SC2 and  $d$  its thickness:

$$\sin \theta d\theta d\phi = \frac{(d + h - Z)}{((x - X)^2 + (y - Y)^2 + (d + h - Z)^2)^{\frac{3}{2}}} dx dy \quad (66)$$

$$\frac{d\Gamma}{dx dy} = \frac{1}{4\pi\tau^+} \left[ 1 \pm \frac{(d + h - Z) \cdot \xi \cos \omega t}{3\sqrt{(x - X)^2 + (y - Y)^2 + (d + h - Z)^2}} \right] \frac{(d + h - Z)}{((x - X)^2 + (y - Y)^2 + (d + h - Z)^2)^{\frac{3}{2}}}$$

Note that the integration is performed over  $x$  and  $y$ , so we get  $\Gamma = \Gamma(X, Y, Z)$ . Assuming that the probability of muon decay is constant in SC2 volume  $dP = V^{-1} dX dY dZ$ , we can integrate  $\Gamma(X, Y, Z)$  on the domain of  $X, Y, Z$ :

$$\Gamma = \frac{1}{\Delta X \Delta Y \Delta Z} \int_{X_{min}}^{X_{max}} \int_{Y_{min}}^{Y_{max}} \int_{Z_{min}}^{Z_{max}} \Gamma(X, Y, Z) dX dY dZ \quad (67)$$

Having different gaps between SC1-SC2 ( $h^{up} = 1.95$  cm) and SC2-SC3 ( $h^{down} = 0.5$  cm):

$$\begin{cases} \Gamma^{up}(t) = \frac{1}{\tau^+} (0.187863 + 0.034509 \cdot \xi \cos \omega t) \\ \Gamma^{dw}(t) = \frac{1}{\tau^+} (0.194805 - 0.034640 \cdot \xi \cos \omega t) \end{cases} \quad (68)$$

Thus, the relations reported in Eq.60, 61 and 62 can be modified in order to take into accounts these geometric effects:

$$\Gamma(t)^{up} = \frac{1}{\tau^+} [a^{up} + b^{up} \cdot \xi \cos \omega t] \quad \Gamma(t)^{dw} = \frac{1}{\tau^+} [a^{dw} - b^{dw} \cdot \xi \cos \omega t]$$

$$U(t) = \frac{N_0}{\tau^+} [a^{up} + b^{up} \cdot \xi \cos \omega t] e^{-t/\tau^+} \quad D(t) = \frac{N_0}{\tau^+} [a^{dw} - b^{dw} \cdot \xi \cos \omega t] e^{-t/\tau^+} \quad (69)$$

- As said in Sec.6, through the aforementioned apparatus we want to detect only muons decayed in SC2. However, if a muon passes SC1 and SC2, decays between SC2 and SC3 (start topology) and if the decay  $e^\pm$  is enough energetic ( $E_{max} = m_\mu/2$ ) to cross SC2 and SC1 (up-stop topology), we measure a up event with a decay out of the magnetic field. To consider this effect we have to add to  $U(t)$  of Eq.69 the distribution of free decaying muons:

$$U(t) = \frac{N_0}{\tau^+} [a^{up} + b^{up} \cdot \xi \cos \omega t] e^{-t/\tau^+} + \frac{N_0}{\tau^+} \cdot \tilde{c} \cdot e^{-t/\tau^+}$$

Integrating  $U(t)$  and  $D(t)$  of Eq.69 in the time range  $[0, 9]\mu s$ , we can estimate  $\tilde{c}$  value from data total number of events  $N_{exp}^{up}$  and  $N_{exp}^{dw}$ :

$$\frac{N_{exp}^{up}}{N_{exp}^{dw}} = \frac{N_0/\tau^+ \int_0^9 ([a^{up} + b^{up} \cdot \xi \cos \omega t] e^{-t/\tau^+} + \tilde{c} \cdot e^{-t/\tau^+}) dt}{N_0/\tau^+ \int_0^9 [a^{dw} - b^{dw} \cdot \xi \cos \omega t] e^{-t/\tau^+} dt} \rightarrow \tilde{c} = 0.074379$$

Finally, we can merge  $\tilde{c}$  in  $a^{up}$  obtaining the following result:

$$a^{up} = 0.262242 \quad (70)$$

- A small depolarization of muons is expected as a result of a macroscopic magnetic field non uniformity. Therefore the polarization changes [10]:

$$\boxed{\xi(t) = \xi_0 \frac{\sin \frac{\Delta\omega}{2} t}{\frac{\Delta\omega}{2} t}} \quad (71)$$

where  $\Delta\omega$  is the mean  $\omega$  variation from the nominal value:  $\Delta\omega = \sigma_\omega = 0.043$  MHz. Since  $\Delta\omega$  is very small:

$$\frac{\sin \frac{\Delta\omega}{2} t}{\frac{\Delta\omega}{2} t} \approx 1$$

for all  $t \in [0, 9]\mu s$ , this effect can be neglected.

- A priori*, it's necessary to consider the bound-decaying  $\mu^-$  represented by  $\frac{N_0^b}{2\tau^-} e^{-t/\tau^-}$  [10]. This term should be added to both  $U(t)$  and  $D(t)$  of Eq.69 as binding the muon loses its polarization and the electron has an equal probability to go up or down. Since in carbon  $\tau^+ \approx \tau^-$  and  $\mu^-$  cannot be distinguished from  $\mu^+$ , this term gives a further correction to  $a^{up}$  and  $a^{dw}$  that we don't estimate.
- Another systematic is represented by the free mean path of  $e^\pm$ , in fact we should weight  $e^\pm$  phase space by its escape probability function which depends on  $E/E_{max}$ ,  $\cos \theta$  and  $Z$ . Unfortunately, this systematic can't be evaluated by a simple model, so we don't consider it.

The theoretical estimation of  $a^{up}$ ,  $a^{dw}$ ,  $b^{up}$  and  $b^{dw}$  are listed in Tab.3. Finally, thanks to this systematic corrections, the asymmetry becomes:

$$A(t) = \frac{(a^{up} - a^{dw}) + \xi(b^{up} + b^{dw}) \cos \omega t}{(a^{up} + a^{dw}) + \xi(b^{up} - b^{dw}) \cos \omega t}$$

Since  $b^{up} \approx b^{dw}$ :

$$A(t) \approx \frac{a^{up} - a^{dw}}{a^{up} + a^{dw}} + \xi \cdot \frac{b^{up} + b^{dw}}{a^{up} + a^{dw}} \cos \omega t$$

| $a^{up}$ | $a^{dw}$ | $b^{up}$ | $b^{dw}$ |
|----------|----------|----------|----------|
| 0.262242 | 0.194805 | 0.034509 | 0.034640 |

Table 3: *Values of asymmetry parameters after systematic studies.*

Defining:

$$\eta = \frac{a^{up} - a^{dw}}{a^{up} + a^{dw}} \quad \rho = \frac{b^{up} + b^{dw}}{a^{up} + a^{dw}} \quad (72)$$

the expected asymmetry becomes:

$$A(t) = \eta + \xi\rho \cos\omega t \quad (73)$$

Substituting in Eq.72 the values reported in Tab.3, we get the following theoretical prediction of  $\eta$  and  $\rho$ :

$$\underline{\eta = 0.147549} \quad \xi \cdot \rho = 0.052953 \quad (74)$$

### 6.2.1 Asymmetry Experimental Result

Using the experimental apparatus described in Sec.6, we have collected a sample of  $n_{tot} = 51675$  decay events subdivided in  $n_{dw} = 21989$  and  $n_{up} = 29686$ . In order to extract the asymmetry parameters ( $\eta$ ,  $\xi \cdot \rho$  and  $\omega$ ) from data, we have to bin the up/down obtained events distributions taking into account the integrated statistics. Thus, the analysis is surely bin dependent. Since the oscillation amplitude is expected to be very small, we have to test if data are compatible with a constant (absence of oscillation), so two least squared method fit are implemented and compared. The goal is to choose the best binning that allows, simultaneously, to obtain an hypothesis test with a good significance for the asymmetry presence (data distributed according to Eq.73) and to exclude, within a good confidence level, the hypothesis of absence of oscillation. Therefore, varying the bin width in the range [120, 700] ns in steps multiples of 20 ns both the constant and the oscillation fit are performed for each of these bin width. Fig.47 shows the normalized  $\chi^2$  trend for the linear and the cosine fit as function of the bin width. For small binning  $\chi^2_0$  for both the hypothesis is closed to one, so with this choice these experimental data are compatible with the presence and the absence of oscillation. On the other hand, for grater values there is a clear separation: the  $\chi^2_0$  values for cosine fit are always less than one, the linear fit values are always grater than one. The best choice consists of a  $\chi^2_0$  value for cosine fit close to one, much grater than one for the linear with the limit that the bin width has not to be large in order to maintain a fine number of degree of freedom ( $n_{df}$  has an important rule in the  $\chi^2$  distribution, see Eq.27). Thus, the optimal bin width chosen is  $\Delta t = 420$  ns, in Fig.48 and Fig.49 the related asymmetry fits for both the hypothesis are shown. These are the obtained

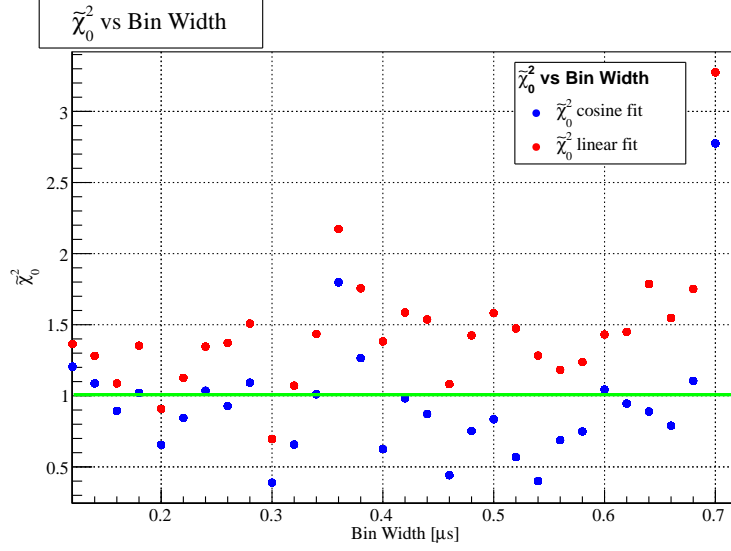


Figure 47: Normalized  $\chi^2$  a for linear and oscillation hypothesis as function of bin width.

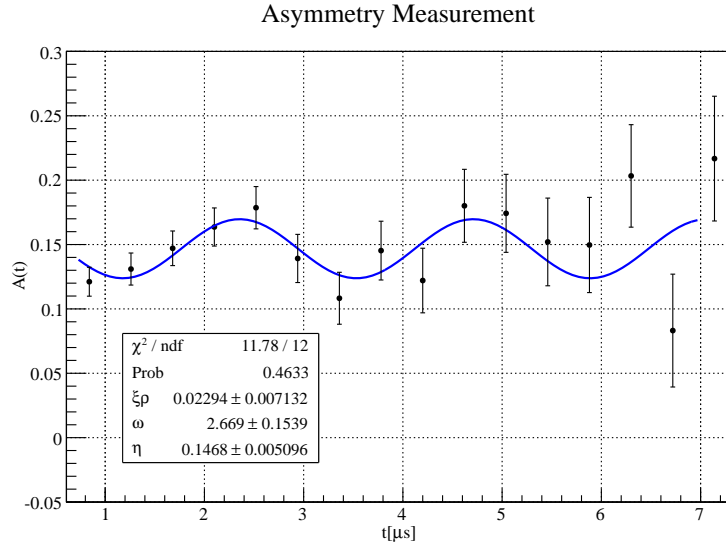


Figure 48: Asymmetry measurement as function of time fitted with the distribution in Eq. 73.

results:

$$\text{Cosine fit : } \xi \cdot \rho = 0.023 \pm 0.007 \quad \eta = 0.147 \pm 0.005 \quad \omega = 2.669 \pm 0.154 \text{ MHz}$$

$$\boxed{\chi_0^2 = \frac{11.78}{12} = 0.98 \quad P(\chi^2 \geq \chi_0^2) = 46.33\% \in 90\% \text{ C.L.}}$$

$$\boxed{\text{Linear fit : } \delta = 0.142 \pm 0.005 \quad \chi_0^2 = \frac{22.2}{14} = 1.58 \quad P(\chi^2 \geq \chi_0^2) = 7.46\% \notin 90\% \text{ C.L.}}$$

As with the binning chosen the  $\chi^2$  linear fit significance is equal to  $s = 7.46\% \rightarrow \text{C.L.} = 1 - s = 92.54\%$  this hypothesis can be excluded fixing a confidence level of 90%. The extracted value for Larmour frequency and the constant  $\eta$  are consistent with the expected ones, reported in

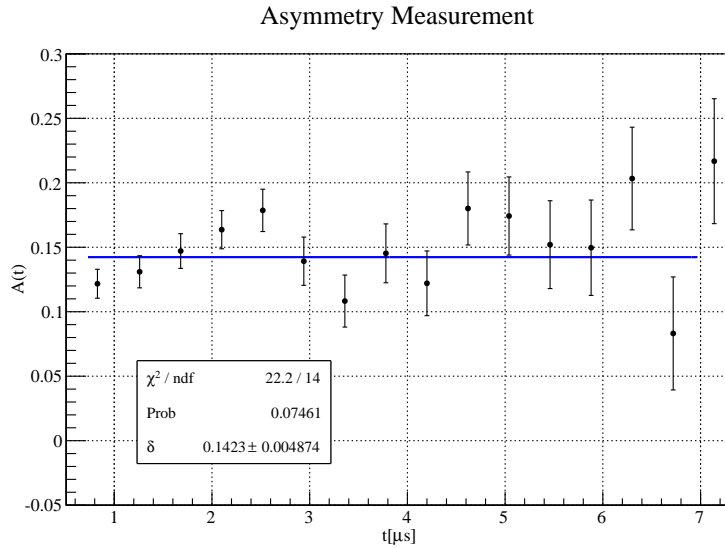


Figure 49: *Asymmetry measurement as function of time fitted with constant function.*

Eq.65 and Eq.74, within a 68% C.L. On the other hand, the amplitude  $\xi \cdot \rho$  values obtained from the fit procedure is not compatible with the expected value reported in Eq.74. The relative difference between  $(\xi \cdot \rho)_{\text{expected}}$  and  $(\xi \cdot \rho)_{\text{fit}}$  is 56.62%; this is probably due to other systematics not included in our estimation of  $a^{up}$ ,  $a^{dw}$ ,  $b^{up}$  and  $b^{dw}$  such as the correction to  $a^{up}$  and  $a^{dw}$  due to the loss of bounded  $\mu^-$  polarization.

In order to eliminate the most of systematics that have effect on our experimental apparatus, we have measured the asymmetry in absence of magnetic field collecting  $n_{up} = 4336$  and  $n_{dw} = 3522$ . Using the same binning of 420 ns, in each bin the asymmetry value measured without the magnetic field is subtracted to the previous one. Unfortunately, the statistic of up/down events in this configuration is not comparable with the one with  $B$  field; this brings to an increase of statistical uncertainties in the subtracted asymmetry distribution shown in Fig.50 and Fig.51.

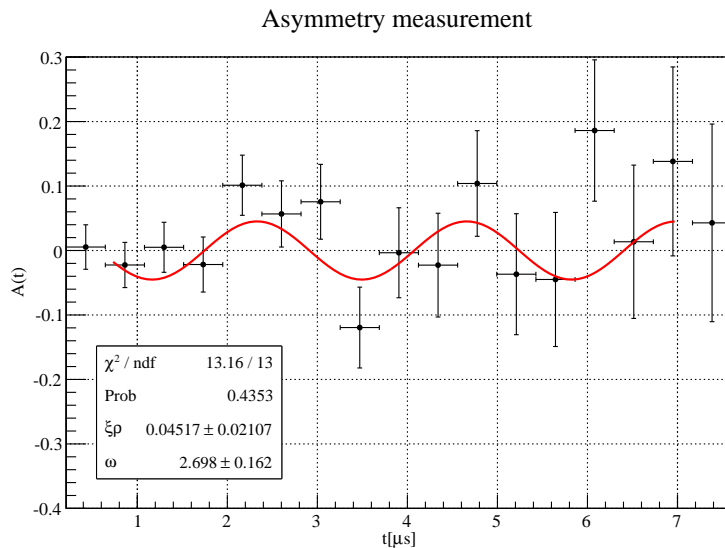


Figure 50: *Subtracted asymmetry as function of time fitted with the distribution in Eq.73.*

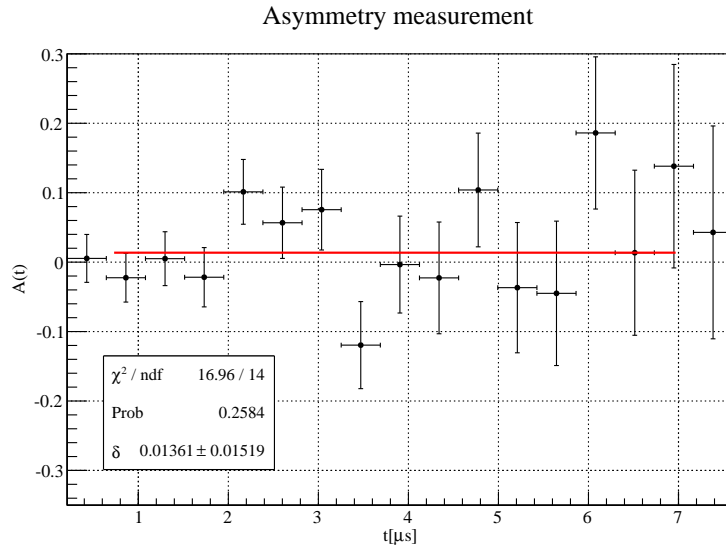


Figure 51: Subtracted asymmetry as function of time fitted with constant function.

These are the obtained results from cosine and linear fit of subtracted distribution:

$$\text{Cosine fit : } \eta = 0 \rightarrow \text{fixed} \quad \xi \cdot \rho = 0.045 \pm 0.021 \quad \omega = 2.698 \pm 0.162 \text{ MHz}$$

$$\boxed{\chi_0^2 = \frac{13.16}{13} = 1.01 \quad P(\chi^2 \geq \chi_0^2) = 43.53\% \in 68\% \text{ C.L.}}$$

$$\boxed{\text{Linear fit : } \delta = 0.014 \pm 0.015 \quad \chi_0^2 = \frac{16.96}{14} = 1.21 \quad P(\chi^2 \geq \chi_0^2) = 25.84\% \notin 68\% \text{ C.L.}}$$

The  $\chi^2$  linear fit significance is equal to  $s = 25.84\% \rightarrow \text{C.L.} = 1 - s = 74.16\%$  this hypothesis can be excluded fixing a confidence level of 68%. The extracted value for Larmour frequency is still consistent with the expected one, reported in Eq.65, within a 68% C.L. The amplitude  $\xi \cdot \rho$  values obtained from the fit is now closer to the expected value reported in Eq.74. Never the less it is estimated with a great statistical uncertainty ( $\approx 50\%$ ) due to low statistic, as already explained.

## A Free muon decay

As already said in Sec.1.2, the differential rate for muon decay is given by:

$$d\Gamma = (2\pi)^4 \delta^4 \left( p_\mu - \sum_f p_f \right) \frac{1}{2E_\mu} \prod_f \frac{d^3 p_f}{(2\pi)^3 2E_f} \sum_f |M|^2$$

where  $f=\{1,2,3\}$  is the final state particles index ( $e$ ,  $\nu_e$  and  $\nu_\mu$ ). The amplitude  $M$  follows from the Feynman rules using the low energy approximation of  $W^\pm$  propagator, i.e.:

$$\frac{-g_{\mu\nu} - \frac{q_\mu q_\nu}{M_W^2}}{q^2 - M_W^2} \rightarrow -\frac{g_{\mu\nu}}{M_W^2} \quad (75)$$

where  $q^2 = (p_\mu - p_{\nu_\mu})^2 = (p_{\nu_e} - p_e)^2$ , we have:

$$M = -\frac{G_f}{\sqrt{2}} \left[ \bar{u}_{r'}(p_{\nu_\mu}) \gamma^\mu (1 - \gamma^5) u_r(p_\mu) \right] \left[ \bar{u}_s(p_e) \gamma_\mu (1 - \gamma_5) v_{s'}(p_{\nu_e}) \right] \quad (76)$$

where  $G_f$  (Fermi constant) is  $1.16637(1) \cdot 10^{-5} \text{ GeV}^{-2}$  [1]. Summing over the final polarizations and mediating on the initial ones, thanks to the trace theorem and in the limit of  $m_{\nu_e} \rightarrow 0$   $m_{\nu_\mu} \rightarrow 0$ , we obtain:

$$\frac{1}{2} \sum_{r,r',s,s'} |M|^2 = \frac{G_f^2}{4} Tr \left[ \not{\psi}_{\nu_\mu} \gamma^\mu (1 - \gamma^5) (\not{\psi}_\mu + m_\mu) \gamma^\nu (1 - \gamma^5) \right] Tr \left[ (\not{\psi}_e + m_e) \gamma_\mu (1 - \gamma_5) \not{\psi}_{\nu_e} \gamma_\nu (1 - \gamma_5) \right]$$

Using the proprieties of  $\gamma$ -matrices  $[\{\gamma^5, \gamma^\mu\}] = 0$ ,  $(1 - \gamma^5)^2 = 2(1 - \gamma^5)$  and traces ones [13], this reduces to:

$$\frac{1}{2} \sum_{r,r',s,s'} |M|^2 = 16G_f^2 \left[ V^{\mu\nu}(p_{\nu_\mu}, p_\mu) V_{\mu\nu}(p_e, p_{\nu_e}) - A^{\mu\nu}(p_{\nu_\mu}, p_\mu) A_{\mu\nu}(p_e, p_{\nu_e}) \right]$$

$$V^{\mu\nu}(p_1, p_2) = p_1^\mu p_2^\nu + p_1^\nu p_2^\mu - g^{\mu\nu}(p_1 \cdot p_2) \quad A^{\mu\nu}(p_1, p_2) = -i\epsilon^{\mu\alpha\nu\beta} p_{1\alpha} p_{2\beta}$$

that gives:

$$\frac{1}{2} \sum_{r,r',s,s'} |M|^2 = 64G_f^2 (p_{\nu_\mu} \cdot p_e) (p_{\nu_e} \cdot p_\mu) \quad (77)$$

Combining Eq.A with Eq.77, we get the unpolarized electron spectrum in function of  $Q = p_\mu - p_e$ :

$$E_e \frac{d\Gamma}{d^3 p_e} = \frac{4G_f^2}{(2\pi)^5 E_\mu} (p_e)^\mu (p_\mu)^\nu I_{\mu\nu} \rightarrow I_{\mu\nu} = \int \frac{d^3 p_{\nu_e}}{E_{\nu_e}} \frac{d^3 p_{\nu_\mu}}{E_{\nu_\mu}} \delta^4(Q - p_{\nu_e} - p_{\nu_\mu}) (p_{\nu_\mu})_\mu (p_{\nu_e})_\nu$$

Following from Lorentz covariance of  $I^{\mu\nu}$ , its most general form is:

$$I^{\mu\nu}(Q) = A(Q^2)(g^{\mu\nu} + 2Q^\mu Q^\nu) + B(Q^2)(g^{\mu\nu} - 2Q^\mu Q^\nu) \quad (78)$$

If we contract the orthogonal tensors  $g^{\mu\nu} + 2Q^\mu Q^\nu$  and  $g^{\mu\nu} - 2Q^\mu Q^\nu$  with  $I_{\mu\nu}$ , we can obtain A and B as follows:

$$B(Q^2) = 0 \quad A(Q^2) = \frac{1}{12} \int \frac{d^3 p_{\nu_e}}{E_{\nu_e}} \frac{d^3 p_{\nu_\mu}}{E_{\nu_\mu}} \delta^4(Q - p_{\nu_e} - p_{\nu_\mu}) \quad (79)$$

Since  $A(Q^2)$  is Lorentz invariant, we can choose the centre of mass system of the two neutrinos ( $\vec{p}_{\nu_\mu} = -\vec{p}_{\nu_e} \rightarrow \vec{Q} = 0$ ), so that:

$$A(Q^2) = \frac{1}{12} \int \frac{d^3 p_{\nu_\mu}}{E_{\nu_\mu}^2} \delta(Q^0 - 2E_{\nu_\mu}) = \frac{\pi}{6} \int \frac{|\vec{p}_{\nu_\mu}|^2}{E_{\nu_\mu}^2} dp_{\nu_\mu} \delta\left(E_{\nu_\mu} - \frac{Q^0}{2}\right) = \frac{\pi}{6} \quad (80)$$

And the electron spectrum becomes:

$$E_e \frac{d\Gamma}{d^3 p_e} = \frac{4G_f^2}{(2\pi)^5 E_\mu} (p_e)^\mu (p_\mu)^\nu I_{\mu\nu} \rightarrow E_e \frac{d\Gamma}{d^3 p_e} = \frac{4G_f^2}{(2\pi)^5 E_\mu} \frac{\pi}{6} \left( Q^2 (p_e \cdot p_\mu) + 2(Q \cdot p_e)(Q \cdot p_\mu) \right) \quad (81)$$

Finally, we have to integrate Eq.81 over the electron momentum  $p_e$  in the rest frame of the muon where  $p_\mu = (m_\mu, \vec{0})$ ,  $\vec{p}_e = -\vec{p}_\mu$  and  $E_e = \frac{m_\mu x}{2}$  with  $x \in [0, 1]$ , obtaining:

$$\Gamma = \frac{2\pi}{3} \frac{G_f^2}{(2\pi)^5 m_\mu} \int p_e dE_e d\Omega \left[ (m_\mu^2 + m_e^2 - 2m_\mu E_e)m_\mu E_e + 2m_\mu(m_\mu - E_e)(m_\mu E_e - m_e^2) \right]$$

If we neglect the electron mass term  $m_e \rightarrow 0$ ,  $p_e \approx E_e = \frac{m_\mu x}{2}$ , we arrive to the Fermi formula:

$$\Gamma = \frac{G_f^2 m_\mu^5}{96\pi^3} \int_0^1 dx x^2 (3 - 2x) = \frac{G_f^2 m_\mu^5}{192\pi^3} \implies \tau[\mu^\pm \rightarrow e + \nu_e + \bar{\nu}_\mu] = 2.2\mu s \quad (82)$$

## B DAQ Software

This code commands and syntax are related to the oscilloscope use in the experiment (Tektronix TDS 2022, 200 MHz, 2 GS/s)

```
#include <c:\programmi\national instruments\measurementstudio\cvi\include\utility.h>
#include <c:\programmi\national instruments\measurementstudio\cvi\include\gpib.h>
#include <c:\programmi\national instruments\measurementstudio\cvi\include\ansi_c.h>
#include <stdio.h>
#include <stdlib.h>
#include <time.h>

#define SCALE_X 1.0E-06           /// X-axis scale (s/div)
#define OFFSET_X -4.0E-06          /// X-scale offset (s)
#define SCALE1_Y 100.0E-3          /// CH1 Y-axis scale (volt/div)
#define OFFSET1_Y 0.0              /// CH1 Y-scale offset (divisions)
#define SCALE2_Y 100.0E-3          /// CH2 Y-axis scale (volt/div)
#define OFFSET2_Y 0.0              /// CH2 Y-scale offset (divisions)
#define TRIGGERLEVEL -100.0E-3
#define Delay 10                  /// Default delay between start and stop (division)

int write (int device , char command[256]) //Function to give commands to the oscilloscope
{
    int sta ;
    sta = ibclr (device) ;
    Delay (0.05) ;
    sta = ibwrt (device , command , strlen (command)) ; // gpib method to write command
    Delay (0.05) ;
    return (sta) ;
}

int read (int device , char string[256]) // Function to read information from the oscilloscope
{
    int j , sta ;
    for (j=0; j<256; ++j) // default initialization
        string[j] = '\000' ;
    sta = ibrd (device , string , 256) ; // gpib method to read information
    printf ("\n%s\n", string) ;
    sta = ibclr (device) ;
    return (sta) ;
}

int main ()
{
    int device , intbuf[256];
    char charbuf[256];
    unsigned char waveForm2[2512]={0} ;
    int amp1=0, amp2=0, ti = -1, tf=-1, doppio=0,doppio_start=0;
    char FileName[50],FileName2[50] ;
    int i , a=10, j , s1=0, s2=0, c=0, u=0,d=0;
    double Te = 0;
    double DeltaT=0;
    int flag=0;
    FILE * outFile , * outFile2;

    Te=Timer();
    printf("tempo_evento: %lf\n", Te);
    device = ibdev (1, 1, NO_SAD, T10s, 1 ,0) ; // initialize device
    ibclr (device) ; // clear oscilloscope buffer
    write (device , "verbose_on") ; // set the oscilloscope in high verbosity mode
    write (device , "*idn?") ; // queries and writes the identifier of the oscilloscope
```

```

read (device , charbuf) ;           /// id and information
write (device , "factory")          /// resets the oscilloscope to defalut settings
write (device , "unlock_all") ;
write (device , "ch1:probe_1") ;     /// set CH1 probe attenuation to 1
write (device , "ch2:probe_1") ;     /// set CH2 probe attenuation to 1

for (i=0; i<256; ++i)      /// Set charbuf to empty vector
{charbuf[ i ] = '\000';}
sprintf (charbuf , "horizontal:main:scale_%e" , SCALE_X);      /// Set X-axis main scale
write (device , charbuf) ;
for (i=0; i<256; ++i)
{charbuf[ i ] = '\000';}
sprintf (charbuf , "horizontal:main:position_%e" , OFFSET_X);  /// Set X-axis offset and
write (device , charbuf) ;
for (i=0; i<256; ++i)
{charbuf[ i ] = '\000';}
sprintf (charbuf , "ch2:scale_%e" , SCALE2_Y);    /// set CH2 Y-axis scale
write (device , charbuf) ;
for (i=0; i<256; ++i)
{charbuf[ i ] = '\000';}
sprintf (charbuf , "ch2:position_%e" , OFFSET2_Y);   /// and CH2 Y-axis offset
write (device , charbuf) ;
for (i=0; i<256; ++i)
{charbuf[ i ] = '\000';}
sprintf (charbuf , "ch1:scale_%e" , SCALE1_Y);    /// set CH1 Y-axis scale
write (device , charbuf) ;
for (i=0; i<256; ++i)
{charbuf[ i ] = '\000';}
sprintf (charbuf , "ch1:position_%e" , OFFSET1_Y); // set CH1 Y-axis offset
write (device , charbuf) ;

write (device , "trigger:main:edge:source_ext") ;  /// Set the trigger source
write (device , "trigger:main:edge:slope_fall") ;   /// Set of trigger modes on edge slope fall
for (i=0; i<256; ++i)
{charbuf[ i ] = '\000';}
sprintf (charbuf , "trigger:main:level_%e" , TRIGGERLEVEL) ; // set a default trigger level
write (device , charbuf) ;

write (device , "data:encdg_rpbinary"); //Set of data encoding rpbinary , width 1
write (device , "data:width_1");
write (device , "data:start_1"); // Set number of sampled points for each waveform (2500)
write (device , "data:stop_2500");
write (device , "select:ch1_on"); // Turn on CH1
write (device , "select:ch2_on"); // Turn on CH2
write (device , "acquire:mode_sample"); // Set acquisition sample mode with stopafter sequence
write (device , "acquire:stopafter_sequence");
sprintf (FileName , "C:\\2010-2011\\MuLibero\\Tempo.Libero.txt"); // Create name of output file
sprintf (FileName2 , "C:\\2010-2011\\MuLibero\\CH_2.txt");
printf("\n*mu->e-*\n");
printf("*****\n");
write (device , "acquire:state_run"); // Set state of the oscilloscope ready to acquire
                                         //with the settings preaviously chosen
printf("Oscilloscope_up_and_ready\n");
Te = Timer();
printf("tempo_evento: %lf\n" , Te);           /// Time taken fo settings

while(1)
{      /// infinite loop waiting for a trigger event
  write (device , "trigger:state?") ;
  ibrd(device , intbuf , 256) ; // Read information about the trigger state
  if (intbuf[4]==172316225)

```

```

{
++c;                                // Good external trigger event
printf("n_e : %d\n", c);
Te = Timer();                         // Absolute time of the event
printf("t_e : %lf\n", Te);
write (device, "data:source=ch1") ;    // Set CH1 as data source
write (device, "curve?") ;
ibrd (device, waveForm2, 2512) ;      // Acquire complete waveform on CH1
outFile = fopen (FileName,"a+") ;     // Open the output file keeping old data
outFile2 = fopen (FileName2,"a+") ;
//fprintf(outFile , "%d ", c);
//fprintf(outFile2 , "%d ", c);

///START EVENT ANALYSIS
for (s2=0,i=13; i<2512; ++i) // Cycle on waveform points (2500->resolution 4ns)
{ if( ((int) waveForm2[i]) < 77) && s2 == 0) // On Y-axis 1 volt -> 255 division.
{   //So we are looking for a point on the waveform under the trigger threshold on CH1.
   //It depends on which scintillator in our measure
   // in connected with CH1 and it is equal to the threshold of the discriminator
s2=i;
a=i; // save time and amplitude information of this point
amp1 = waveForm2[i];
for (j=i+1; j<i+17 && j<2512; ++j) // waveform control goodness.
{ if(waveForm2[j] < amp1)a
  amp1 = waveForm2[j];
  if(waveForm2[j]>waveForm2[i]&&flag==0)
  { flag=1;
    ti=s2;
  } // here we control if in the next 100 ns the waveform drops under the trigger level.
} // so we can control the tail Pile-up
}
flag=0;
s2=0;

/// SEARCHING FOR UP STOP EVENTS
for(i=2220; i < 2250; i++) // Searching on CH1 near the "trigger position" a stop signal
{ if( ((int) waveForm2[i]) < 77 &&s2==0) // Condition for a possible stop event
{s2=1;
amp2 = waveForm2[i];
for (j=i+1; j<i+17 && j<2512; ++j) // waveform control goodness.
{ if(waveForm2[j] < amp2)
  amp2 = waveForm2[j];
  if(waveForm2[j]>waveForm2[i] &&flag==0)
  { printf("up\n"); //signal compatible with up event
    u=1;
    flag=1;
    tf=i; // time of the stop
  }
}
}
write (device, "data:source=ch2") ;      // Set CH2 as data source
write (device, "curve?") ;
ibrd (device, waveForm2, 2512) ;        // Acquire complete waveform on CH2
fprintf(outFile2 , "_CH2_\n");
for (i=13; i<2512; ++i)               // Save complete waveform on CH2
{s2=(int) waveForm2[i];
 fprintf(outFile2 , "%d-",s2);
}

/// SEARCHING FOR DOUBLE START EVENT

```

```

s2=0;
for (i=a-10; i<a+10; i++) //Cycle around the start position in a range of ± 40ns
{ if ( ((int) waveForm2[ i ]) < 115&&s2==0) // threshold level for a double start event
 { doppio_start=1; // save information of double start event
   s2=1;
   printf("doppio_start\n");
 }
 flag=0;
 s2=0;

///SEARCHING FOR DOWN STOP EVENT and DOUBLE STOP EVENT
for (i=2220; i < 2250; i++) // Searching on CH2 near the "trigger position" a stop signal
{ if ( ((int) waveForm2[ i ]) < 110 &&s2==0) // Threshold condition for a possible stop event
 { s2=1;
   amp2 = waveForm2[ i ];
   for (j=i+1; j<i+17 && j<2512; ++j) // waveform control goodness.
   { if (waveForm2[ j ] < amp2)
     amp2 = waveForm2[ j ];
   if (waveForm2[ j ]>waveForm2[ i ]&& flag==0)
   { printf("down\n"); //signal compatible with down event
     flag=1;
     d=1;
     tf=i; // time of the stop
   }
 }
 if (u==1)
 { doppio=1;
   printf("doppio\n"); // double stop event
 }
 }

if ((u==1&&d==0)|| (u==0&&d==1)|| doppio==1|| doppio_start==1) //conditions saving event
{ if ( ti!= -1&&tf!= -1)
 {DeltaT = ((tf-ti+Delay)*10)/( (double) 2500); //Calculating time between start and stop
  printf("t =%lf\n", DeltaT);
  fprintf(outFile, "%lf ", DeltaT); // Saving in the output file
  fprintf(outFile, "%d ", u);
  fprintf(outFile, "%d ", d);
  fprintf(outFile, "%d ", doppio_start);
  fprintf(outFile, "%d ", doppio);
  fprintf(outFile, "%lf\n", Te);
 }
}

doppio = 0;
doppio_start=0;
u = 0;
d=0;
ti = -1;
tf=-1;
Te = 0;
s2=0;
flag=0;
fclose (outFile); // Closing file
fclose (outFile2);
write (device , "acquire:state_run"); // Set state ready to acquire after a new trigger
printf("-----\n");
}

return (0);
}

```

## References

- [1] K.Nakamura et al.(Particle Data Group). *J. Phys. G* **37**, 075021 (2010).
- [2] et al. O. Adriani. Pamela measurements of cosmic-ray proton and helium spectra. *Science* **332**, 69 (2011);.
- [3] et al. D.J. Bird. The cosmic-ray energy spectrum observed by the fly's eye. *The Astrophysical Journal*, 424:291-502, 1994 March 20;.
- [4] A.O. Weissenberg. “*Muons*”. **North Holland Publisher**.
- [5] R.B. Sutton et al. “*measurement of negative muon lifetimes in light isotopes*” .
- [6] Glenn F. Knoll. “*Radiation Detection and Measurament*”. **John Wiley and Sons**.
- [7] ROOT Reference Guide. <http://root.cern.ch/root/html/doc/TRandom.html>.
- [8] Minuit2 Package. [http://root.cern.ch/root/html518/MINUIT2\\_Index.html](http://root.cern.ch/root/html518/MINUIT2_Index.html).
- [9] W. J. Metzger. “*statistical methods in data analysis*”. **Katholieke Universiteit Nijmegen**.
- [10] R. Turner, C. M. Ankenbrandt, and R. C. Larsen. Polarization of cosmic-ray muons. *Phys. Rev. D*, 4:17–23, Jul 1971.
- [11] L.B. Okun. “*Lepton and Quarks*”. **North Holland**.
- [12] L.D. Landau and E.M. Lifshitz. “*Quantum Mechanics*”. **Volume 3, Third Ediction**.
- [13] F.Mandl and G.Shaw. “*The Quantum Field Theory* ”. **John Wiley and Sons**, Appendix A, Section A.3.